Viscoelastic jet instabilities studied by direct numerical simulations

Mateus C. Guimarães [1] Fernando T. Pinho,[2,3] and Carlos B. da Silva [1,*]

[1]*IDMEC/LAETA, Instituto Superior Técnico, Universidade de Lisboa, 1049-001 Lisboa, Portugal*
[2]*ALiCE, Faculdade de Engenharia, Universidade do Porto, 4200-465 Porto, Portugal*
[3]*CEFT, Faculdade de Engenharia, Universidade do Porto, 4200-465 Porto, Portugal*

Direct numerical simulations of spatially evolving submerged jets with viscoelastic FENE-P fluids at high Reynolds numbers are performed to investigate the development of inertioelastic shear-layer and jet-column instabilities. An analysis of the flow structures, mean and fluctuating velocities, and spectra of perturbation energy at several positions of the flow shows that viscoelasticity has a destabilizing effect at the linear region of perturbation growth but a stabilizing effect at the nonlinear regime. At the linear regime, shorter waves are destabilized first and as the Weissenberg number Wi is increased this effect is propagated towards longer waves until most modes become more unstable. The frequency domain of instability is increased by a factor larger than four for the jet at the highest Wi. At the nonlinear regime, thin sheets of highly stretched polymers at the shear-layer region lead to a suppression of the local velocity gradient and to the formation of additional inflection points in the base flow velocity profile. This is accompanied by lower rates of perturbation growth and a decrease of the characteristic Strouhal number of the jet column mode at the end of the potential core by a factor of 1.8 for the highest Wi jet. The physical mechanisms that explain the observed phenomena are offered but the need for a nonlinear stability theory that also accounts for nonparallel base flow effects is highlighted.

I. INTRODUCTION

The presence of polymer additives can have a strong influence on the evolution of instabilities in free shear-layers. Linear stability analyses of temporally evolving mixing-layers and jets reveal that, in the limit of infinite Reynolds and Weissenberg numbers with the elasticity number kept of order unity, viscoelasticity is typically stabilizing [1,2]. In this limit condition, viscous diffusion of momentum and polymer relaxation are neglected. However, spatiotemporal linear analysis under more general conditions shows a more complex scenario where viscoelasticity can also have a destabilizing effect on the growth of the perturbations [3,4]. Numerical simulations of mixing-layers at low Reynolds numbers have shown destabilization at the linear regime but stabilization at the nonlinear regime [5]. This dual character of viscoelasticity has also been observed in recent experimental studies of axisymmetric and planar jets with polyethylene solutions [6,7].

The first direct numerical simulations (DNS) of turbulent viscoelastic jets have been performed only recently by Guimarães *et al.* (2020) [8], where the focus was on the statistics at the far-field fully turbulent region of the flow and on the development of a similarity theory for that region, which was later extended to turbulent wakes with small velocity deficits [9]. Here we perform some new DNS of spatially evolving submerged jets with viscoelastic fluids in order to study the evolution of the instabilities at the transition region of the flow. Both linear and nonlinear regions of instability

---

*carlos.silva@tecnico.ulisboa.pt

growth are analyzed. The goal is to assess whether viscoelasticity has a stabilizing or destabilizing influence and to characterize the flow features associated with it. Even though some interesting physics has been recently discovered in the regime of low Reynolds and order unity elasticity numbers [6,7], the focus here will be in the high-Reynolds-number regime that is typical in industrial and engineering applications involving dilute polymer solutions, such as turbulent jet cleaning and cutting operations [10–12], irrigation [13,14], aerial firefighting, turbulent drag reduction in ships [15,16], pipes [17], and large district heating and cooling systems [18].

After a description of the numerical methods and simulation parameters in Sec. II, the results are shown in Sec. III, the physical mechanisms of the instability are discussed in Sec. IV, and conclusions are given in Sec. V.

II. DIRECT NUMERICAL SIMULATIONS

A. Governing equations

The rheology of the long-chain, semidilute polymer solutions is characterized by the finitely extensible non-linear elastic constitutive model with Peterlin's approximation, i.e., the FENE-P model of Bird *et al.* (1980) [19], in a slightly modified format due to Sureshkumar *et al.* (1997) [20]. The momentum equation is given by

$$\frac{\partial \boldsymbol{u}}{\partial t} + \boldsymbol{u} \cdot \boldsymbol{\nabla} \boldsymbol{u} = -\frac{1}{\rho}\boldsymbol{\nabla} p + \nu^{[s]}\nabla^2 \boldsymbol{u} + \frac{1}{\rho}\boldsymbol{\nabla} \cdot \boldsymbol{\sigma}^{[p]}, \tag{1}$$

the polymer stress tensor is

$$\boldsymbol{\sigma}^{[p]} = \frac{\rho \nu^{[p]}}{\tau_p}[f(C_{kk})\boldsymbol{C} - \boldsymbol{I}], \tag{2}$$

and the equation for the evolution of the conformation tensor $\boldsymbol{C}$ is

$$\frac{\partial \boldsymbol{C}}{\partial t} + \boldsymbol{u} \cdot \boldsymbol{\nabla} \boldsymbol{C} = \boldsymbol{\nabla} \boldsymbol{u}^T \cdot \boldsymbol{C} + \boldsymbol{C} \cdot \boldsymbol{\nabla} \boldsymbol{u} - \frac{1}{\tau_p}[f(C_{kk})\boldsymbol{C} - \boldsymbol{I}]. \tag{3}$$

The adopted form of the Peterlin function is $f(C_{kk}) \equiv (L^2 - 3)/(L^2 - C_{kk})$ while the fluid incompressibility condition is imposed by the continuity equation

$$\boldsymbol{\nabla} \cdot \boldsymbol{u} = 0. \tag{4}$$

The polymer and solvent zero shear-rate viscosities are $\nu^{[p]}$ and $\nu^{[s]}$, respectively; τ_p is the polymer relaxation time; and L is the maximum length of the polymer dumbbells normalized by their equilibrium radius.

B. Numerical methods

The momentum equation is solved with pseudospectral methods [21], on the normal (y) and spanwise (z) directions, and a sixth-order compact finite-differences scheme [22] on the streamwise (x) direction. A schematic of the flow geometry and the directions of the coordinate axes are displayed in Fig. 1. An explicit third-order Runge-Kutta scheme is used for time marching [23]. The pressure-velocity coupling is handled by a fractional step method [24]. The method of Vaithianathan *et al.* (2006) [25], based on the shock-capturing Kurganov-Tadmor scheme [26], is employed for the conformation tensor equation. This method does not use any artificial numerical diffusion, and we verified that it provides second-order accuracy at more than 98% of the points of the computational domain. More details about the implementation and validation of our code and the adopted numerical methods can be found at Guimarães *et al.* (2020) [8].

Inflow and outflow conditions are imposed at the inlet and outlet boundaries of the domain, respectively. The mean velocity profile at the inlet has a hyperbolic-tangent shape, and the fluctuating component is obtained from a random-number generator, with a prescribed energy spectrum
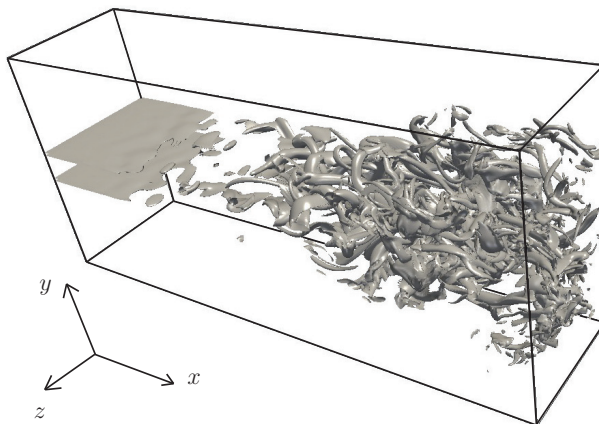
FIG. 1. Schematic of the flow geometry and the directions of the coordinate axes: streamwise (x), normal (y), and spanwise (z) directions. Isosurfaces of vorticity magnitude ($||\boldsymbol{\omega}||$, where the vorticity vector is $\boldsymbol{\omega} = \nabla \times \boldsymbol{u}$) of the Newtonian jet are also displayed, to illustrate our simulations. Two-dimensional contours of $||\boldsymbol{\omega}||$ are shown in Fig. 3, where the origin of the coordinate system is indicated.

characteristic of isotropic turbulence (see Sec. II C). Periodic boundary conditions are imposed at the boundaries facing the transverse and spanwise directions for velocity and conformation tensor components. A nonreflective boundary condition is used at the outlet [27]. The details of the outflow and lateral boundary conditions are given in Appendix A.

C. Physical and computational parameters of the simulations

The velocity field at the inlet is prescribed as the sum of mean and fluctuating components. The mean components are

$$\bar{u}(x = 0, y) = \frac{U_J + U_\infty}{2} + \frac{U_J - U_\infty}{2} \tanh\left[\frac{h}{4\Phi}\left(1 - \frac{2|y|}{h}\right)\right], \tag{5}$$

$$\bar{v}(x = 0, y) = \bar{w}(x = 0, y) = 0, \tag{6}$$

where an overbar denotes a statistical mean made along the homogeneous direction z combined with a temporal average. The origin of the normal coordinate axis ($y = 0$) is placed at the center of the jet.

Two different values of the velocity gradient parameter h/Φ are considered, $h/\Phi = 5$ and 40, in order to study jets with thick and thin shear-layers, respectively. The shapes of these profiles are shown in Fig. 2(a), where only the region $y/h \geqslant 0$ is shown since the profiles are symmetric with respect to the (x, z) plane. For thin shear-layers ($h/\Phi = 40$), U_J is the jet issuing velocity, i.e., $U_c(x = 0) = U_J$, where $U_c(x) = \bar{u}(x, y = 0)$ is the local center-line velocity of the jet. We set $U_J = 1.091$ (arbitrary units) for all cases studied here, which gives $U_c(x = 0) = 1.091$ for jets with $h/\Phi = 40$, and $U_c(x = 0) = 1.0151$ for jets with $h/\Phi = 5$. For all cases, U_∞ is a small coflow velocity that is equal to 0.091 (arbitrary units) at the inlet. For thin shear-layers ($h/\Phi = 40$), h is the slot width of the jet. The same interpretation is used for thick shear-layers ($h/\Phi = 5$), even though Fig. 2(a) shows that for those cases $\bar{u}$ approaches zero only at $y/h \approx 1$ instead of $y/h \approx 0.5$.

The length scale Φ is related to the momentum thickness of the jet θ, which is defined here by the following equation:

$$\theta = \int_{-\infty}^{\infty} \frac{\bar{u} - U_\infty}{U_c - U_\infty}\left(1 - \frac{\bar{u} - U_\infty}{U_c - U_\infty}\right)dy. \tag{7}$$
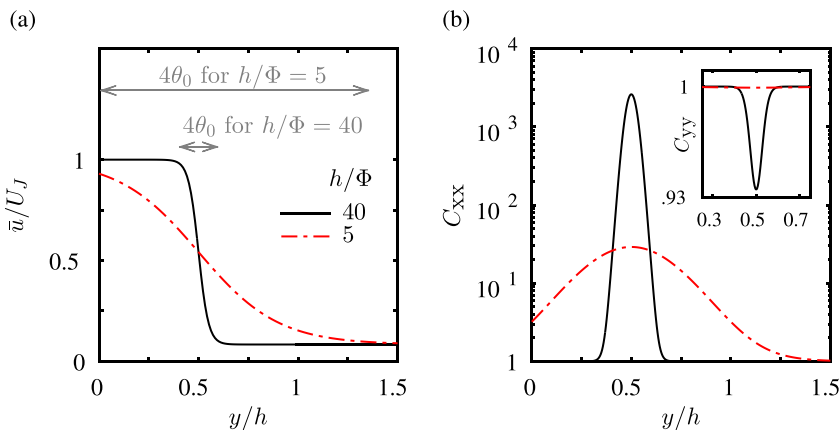
FIG. 2. Transverse profiles of normalized inlet mean velocity (a), first and second normal components of the conformation tensor at the inlet (b) for jets with thin ($h/\Phi = 40$) and thick ($h/\Phi = 5$) shear-layers. The size of the inlet momentum thickness (multiplied by four and divided by h) of each profile is also indicated in panel (a).

For jets with $h/\Phi = 40$, $\Phi = 0.5\theta_0$, whereas for jets with $h/\Phi = 40$, $\Phi \approx 0.587\theta_0$, where $\theta_0 = \theta(x = 0)$. Figure 2(a) displays a schematic of the momentum thickness that shows that θ_0 scales with the thickness of the shear-layer, with a proportionality factor of approximately four.

The fluctuating components of velocity are described by a broadband white noise, without any deterministic forcing, that has an energy spectrum characteristic of isotropic turbulence. The procedure to generate the fluctuating components at the inlet starts in Fourier space and makes use of the following expression:

$$\widehat{u'} = \widehat{v'} = \widehat{w'} \sim (1 + i)\kappa^{s/2} \exp\left[-\frac{(s+2)}{4}\left(\frac{\kappa}{\kappa_p}\right)^2\right], \tag{8}$$

where $i = \sqrt{-1}$ is the imaginary unit, $\kappa = (\kappa_y^2 + \kappa_z^2)^{1/2}$ is the wave-number norm in the (y, z) plane, the upper hat indicates a variable in Fourier space, and a prime indicates a fluctuating component [e.g., the instantaneous streamwise velocity is $u(x, y, z, t) = \bar{u}(x, y) + u'(x, y, z, t)$]. The coefficient that converts the proportionality sign into an equality is obtained from a pseudorandom number generator, and its value varies for each time step. The time-averaged turbulent kinetic energy spectrum that results from Eq. (8) is

$$E(\kappa) \sim \kappa^s \exp\left[\frac{-s}{2}(\kappa/\kappa_p)^2\right]. \tag{9}$$

We set $s = 4$, corresponding to a Batchelor spectrum at the infrared region [28], and the peak wave number κ_p is chosen according to the characteristic frequency of the jet shear-layer mode of instability, as in Stanley *et al.* (2002) [29], described below.

Defining the peak temporal frequency of the inlet noise by $f_{in} = [(U_J + U_\infty)/2]\kappa_p/(2\pi)$, the Strouhal number of the inlet noise by $St_{in} = 2f_{in}\Phi/(U_J + U_\infty) = \kappa_p\Phi/(2\pi)$, and the Strouhal number of the instabilities by $St = 2f_{in}\theta_0/(U_J + U_\infty) = \kappa_p\theta_0/(2\pi)$, we have $St = 2St_{in}$ for thin shear-layers. We compared the results from two Newtonian DNS that use different values of St_{in}: (i) $St_{in} = St/2 = 0.033$, corresponding to twice the frequency of the most unstable mode, and (ii) $St_{in} = St/2 = 0.160$, a frequency that is four times higher than the neutral frequency, i.e., that is associated with a damped mode. For $St_{in} = 0.033$, nonlinear saturation of the fluctuating velocity sets in earlier, about $1.5h$ before the location corresponding to the DNS with $St_{in} = 0.160$, but the growth rates of the instability modes at the linear region of perturbation growth are not affected

TABLE I. Physical parameters of the DNS: inlet Reynolds number [Re $= (U_J - U_\infty)h/\nu^{[s]}$], inlet Weissenberg number [Wi $= \tau_p(U_J - U_\infty)/h$], inlet elasticity number [El $= (1 - \beta)$Wi/Re], Strouhal number of the inlet noise [St$_\text{in} = \kappa_p \Phi/(2\pi)$], inlet condition used for the conformation tensor (Couette flow solution or isotropic tensor), inlet mean velocity parameter (h/Φ), grid spacing normalized by the slot width of the jet ($\Delta x/h$), grid spacing normalized by the Kolmogorov length scale ($\Delta x/\eta$, the maximum value is shown), dimensions of the computational domain on each spatial direction (L_x, L_y, and L_z) normalized by h, and number of grid points on each spatial direction (n_x, n_y, and n_z).

Re	Wi	El	St$_\text{in}$	$\boldsymbol{C}_\text{in}$	$\dfrac{h}{\Phi}$	$\dfrac{\Delta x}{h}$	max$\left\|\dfrac{\Delta x}{\eta}\right\|$	$\dfrac{L_x}{h} \times \dfrac{L_y}{h} \times \dfrac{L_z}{h}$	$n_x \times n_y \times n_z$
1200	0	0	0.160	NA	30	0.07	2.9	$18 \times 18 \times 4.5$	$256 \times 256 \times 64$
1200	0	0	0.033	NA	30	0.07	3.7	$18 \times 18 \times 4.5$	$256 \times 256 \times 64$
1500	0	0	0.033	NA	40	0.02	1.5	$18 \times 18 \times 4.5$	$768 \times 768 \times 192$
1500	1	1.3×10^{-4}	0.033	Couette	40	0.02	1.2	$18 \times 18 \times 4.5$	$768 \times 768 \times 192$
1500	2	2.7×10^{-4}	0.033	Couette	40	0.02	1.1	$18 \times 18 \times 4.5$	$768 \times 768 \times 192$
1500	4	5.3×10^{-4}	0.033	Couette	40	0.02	0.9	$18 \times 18 \times 4.5$	$768 \times 768 \times 192$
1500	4	5.3×10^{-4}	0.033	Isotropic	40	0.02	1.0	$18 \times 18 \times 4.5$	$768 \times 768 \times 192$
1500	0	0	0.033	NA	5	0.03	1.3	$48 \times 48 \times 9$	$1536 \times 1536 \times 288$
1500	4	5.3×10^{-4}	0.033	Couette	5	0.03	1.1	$36 \times 36 \times 9$	$1152 \times 1152 \times 288$
1500	8	10.7×10^{-4}	0.033	Couette	5	0.03	1.0	$48 \times 48 \times 9$	$1536 \times 1536 \times 288$

by the value of St$_\text{in}$. In particular, the Strouhal number of the most unstable mode that is obtained from our Newtonian DNS results is always St $= 0.033$, also for the case where the inlet noise is set with a κ_p that corresponds to St$_\text{in} = 0.160$ (see the inset of Fig. 9 in Sec. III), in agreement with experiments and linear stability calculations [30–33], attesting that the adopted broadband white noise allows for a natural transition of the jet, which is the same conclusion of previous works that make use of this approach [29,34–36].

Using a convolution step function [34], the maximum amplitude of velocity fluctuations at the inlet is set to 1% of U_J, at the lower and upper shear-layers, at $-0.8 \leqslant y/h \leqslant -0.2$ and $0.2 \leqslant y/h \leqslant 0.8$, respectively, and to 0.25% of U_J at the center of the jet, at $-0.2 < y/h < 0.2$. Zero fluctuations are set elsewhere, i.e., at the free stream region.

The inlet Reynolds number is Re $= (U_J - U_\infty)h/\nu^{[s]}$, the ratio of zero shear rate viscosities is $\beta = \nu^{[s]}/(\nu^{[s]} + \nu^{[p]})$, the inlet Weissenberg number is defined as Wi $= \tau_p(U_J - U_\infty)/h$ and the elasticity number is given by El $= (1 - \beta)$Wi/Re. We set $\beta = 0.8$ and $L = 200$ for all viscoelastic DNS. A summary of the physical parameters of the DNS is displayed in Table I, where $\boldsymbol{C}_\text{in}$ indicates the type of the inlet condition used for the conformation tensor (see below). In our DNS we increase the level of viscoelasticity by increasing the inlet Weissenberg number Wi.

In order to simulate distinct operational conditions that might be encountered in applications, we use two different inlet conditions for the conformation tensor. The fully developed laminar Couette flow solution of the FENE-P fluid [37], considering the local value of the mean velocity gradient at each grid point, and a uniform isotropic conformation tensor, i.e., $\boldsymbol{C}_\text{in} = \boldsymbol{I}$. The FENE-P Couette flow solution is obtained by inserting Eqs. (5) and (6) into Eq. (3), imposing zero derivatives in the streamwise and spanwise directions ($\partial/\partial x = \partial/\partial z = 0$) and a steady-state condition ($\partial/\partial t = 0$) with zero fluctuating components. This solution was derived for the first time by Sureshkumar *et al.* (1997) [20], it is a particular case of more general expressions obtained in Pinho *et al.* (2008) [37] and has been adopted in linear stability analysis of viscoelastic jets and mixing-layers [3,4].

For thin shear-layer jets, at the inlet centerline ($x/h = 0$, $y/h = 0$) where the mean velocity gradient is zero, the isotropic and Couette flow conditions give the same result, e.g., $C_{ii} = 3$, but very different levels of polymer stretching are obtained at the shear-layer region. For example, for Wi $= 4$ and $h/\Phi = 40$, the Couette flow solution gives $C_{ii} = 2616$ at $y/h = 0.5$ while the isotropic condition gives $C_{ii} = 3$ everywhere. Figure 2(b) displays transverse profiles of C_{xx} and $C_{yy} = C_{zz}$ of

the Couette flow solution, for viscoelastic jets with thin and thick shear-layers, showing the influence of the velocity gradient parameter h/Φ. At the shear-layer, the polymers are highly stretched on the x direction but slightly compressed on the y and z directions. Throughout the text, when we do not state explicitly which inlet condition is used for $\boldsymbol{C}$, the Couette flow solution is the one in consideration.

For jets with Re $= 1500$ and $h/\Phi = 40$, the number of collocated grid points on each spatial direction of the uniform mesh is $n_x = 768$, $n_y = 768$, and $n_z = 192$ with corresponding domain sizes given by $L_x = L_y = 18h$ and $L_z = 4.5h$. The two Newtonian DNS with Re $= 1200$ (see Table I) use $n_x = 256$, $n_y = 256$, and $n_z = 64$ and the same domain sizes of the other DNS. They were performed to study the influence of the inlet noise on the transition of the jet and the main conclusions were already discussed above. Thus, the results of these two Newtonian DNS will not be discussed further; only a brief reference will be made in Sec. III. For jets with Re $= 1500$ and $h/\Phi = 5$, two DNS with $n_x = n_y = 1536$, $n_z = 288$, $L_x = L_y = 48h$, and $L_z = 9h$ and one DNS with $n_x = n_y = 1152$, $n_z = 288$, $L_x = L_y = 36h$, and $L_z = 9h$ were performed. Our domain size validation study described in Appendix C demonstrates that the computational domains of our DNS are sufficiently large to allow the normal flow development of the jet. Appendix D shows that our simulations are sufficiently large to reach the fully-turbulent far-field and therefore cover the whole transition region.

The grid resolution can be quantified by the ratio of the grid spacing and the slot width, $\Delta x/h$, and also by the ratio of the grid spacing and the Kolmogorov length scale, $\Delta x/\eta$, where $\eta = (\nu^{[s]^3}/\varepsilon^{[s]})^{1/4}$, $\varepsilon^{[s]} = 2\nu^{[s]}\overline{S'_{ij}S'_{ij}}$ is the mean rate of dissipation of turbulent kinetic energy of the solvent, and $S'_{ij} = (\partial u'_i/\partial x_j + \partial u'_j/\partial x_i)/2$ is the fluctuating rate-of-strain tensor. The values of $\Delta x/h$ and $\max|\Delta x/\eta|$ from all simulations are listed in Table I, where $\max|\Delta x/\eta|$ is the maximum value of $\Delta x/\eta$, i.e., $\Delta x/\eta$ evaluated at the position with the poorest resolution. The grid resolution of our DNS with Re $= 1500$ is considerably finer than what is typically used in DNS of spatially evolving Newtonian jets with spectral/compact accuracy [29,34–36], and the excellent level of qualitative and quantitative agreement between our DNS and experimental results, described later in Sec. III, confirms that our simulations are well resolved. This is demonstrated with an extra level of confidence in our grid resolution study, presented in Appendix B.

III. VISCOELASTIC JET INSTABILITIES

This section describes the influence of viscoelasticity on inertioelastic shear-layer and jet-column instabilities at both linear and nonlinear regimes of perturbation growth. This is done in physical space in Sec. III A and in Fourier space in Sec. III B. Section III C discusses the divergence of the base state, which becomes significant for large Wi jets, and Sec. III D reports and explains the differences that exist between jets with thin and thick shear-layers at the inlet.

At some instances we compare our DNS results of planar jets with experimental and theoretical results from round jets. This is justified for thin shear-layers, where the thickness of the shear-layer is much smaller than the radius of the jet and curvature effects are negligible [38,39], except for very long waves. However, for thick shear-layer jets, such as those discussed in Sec. III D, some comparisons between the round and planar configurations can still be made but only qualitatively.

A. Vorticity, mean, and perturbation velocities in physical space

Two-dimensional contours of instantaneous vorticity magnitude at fixed z slices are shown in Fig. 3, where as before the vorticity $\boldsymbol{\omega}$ is defined in the classical way, i.e., $\boldsymbol{\omega} = \nabla \times \boldsymbol{u}$. It is instructive to analyze these results in parallel with those of Fig. 4, showing the streamwise evolution of the root-mean-squared (rms) velocity fluctuation $\sqrt{\overline{u'^2}}$ normalized by the mean velocity difference $U_c - U_\infty$, both evaluated at the jet centerline $y = 0$, and of $[(U_c - U_\infty)/(U_J - U_\infty)]^{-2}$, i.e., the centerline mean velocity normalized according to the self-similarity theory of the far-field [8]. Videos of the flows corresponding to Fig. 3(a) and 3(b) are provided as Supplemental Material [40].
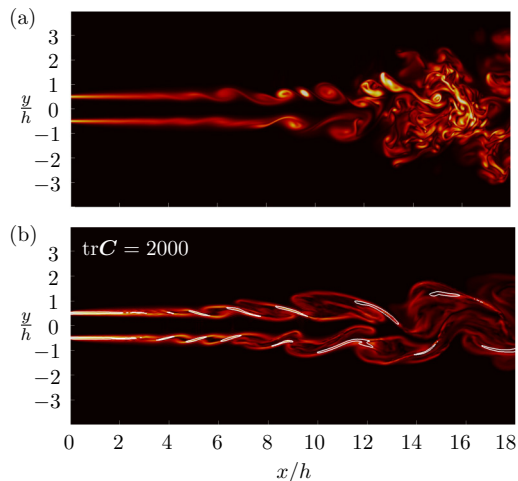
FIG. 3. Two-dimensional contours of instantaneous vorticity magnitude at the middle plane ($z/h = 0$) for (a) Newtonian, and (b) viscoelastic jet with Wi $= 4$. For the viscoelastic jet, isolines of instantaneous polymer stretching $C_{ii} = 2000$ are also shown.

Considering the Newtonian jet first, it can be seen that at $0 < x/h \lesssim 4.5$ velocity fluctuations are much smaller than the mean velocity [Fig. 4(a)] and the vorticity is concentrated in flat sheet structures at the lower ($y/h = -0.5$) and upper ($y/h = 0.5$) shear-layers [Fig. 3(a)]. This is characteristic of a linear region of instability growth. At $x/h \approx 4.5$, the shear-layers start to roll-up [Fig. 3(a)] and the velocity fluctuations grow at a considerably larger rate [Fig. 4(a)], indicating nonlinear growth of instabilities at $x/h > 4.5$, as will be confirmed later in Sec. III B. The end of the potential core is at $x/h \approx 8.5$, where the centerline mean velocity starts to decay [Fig. 4(b)] and at $x/h \approx 15$ there is a peak in the $\sqrt{\overline{u'^2}}/(U_c - U_\infty)$ profile and the flow is very disorganized, displaying a wide range of scales that is characteristic of fully developed turbulence.

From Figs. 3 and 4 it is clear that viscoelasticity has a strong influence on the dynamics described above. For the case with the larger Weissenberg number (Wi $= 4$), the roll-up of the shear-layers starts earlier than the Newtonian case, at $x/h \approx 3.5$ (Fig. 3), indicating a destabilizing viscoelastic effect at the linear region. This destabilizing effect at the linear regime is clearly demonstrated in
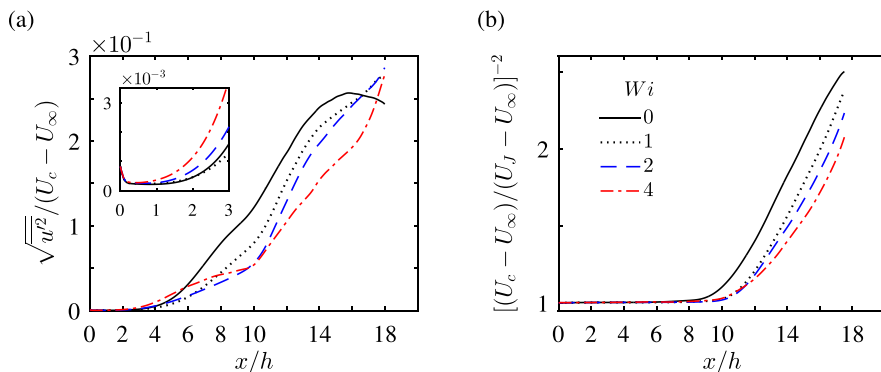

FIG. 4. Streamwise evolution of normalized rms velocity along the centerline (a) and centerline mean velocity difference (b). The inset in panel (a) shows a zoom at $0 \leqslant x/h \leqslant 3$.

the inset of Fig. 4(a), where a zoom at $0 \leqslant x/h \leqslant 3$ shows that as Wi is increased the fluctuating velocities start growing earlier and at a faster rate in comparison to the Newtonian case.

For viscoelastic jets at high Wi, the roll-up of the viscoelastic shear-layers is considerably different from that described by the Newtonian Kelvin-Helmholtz mechanism (Fig. 3). At each shear-layer at $y/h = -0.5$ and $y/h = 0.5$ we can see the presence of two vortex sheets, i.e., in comparison to the Newtonian case additional vortex sheets are formed by viscoelasticity. At each shear-layer, the vortex sheets initially resemble sinusoids with a phase shift of π. This can be seen at Fig. 3(b) at $3.5 \lesssim x/h \lesssim 7$. Further away the sheets do not roll-up completely but are stretched in the direction of the principal strain and become flatter until the final merging of the upper and lower shear-layers at $x/h \approx 11$. This indicates a stabilizing effect of viscoelasticity at the nonlinear region. Indeed, at $4 \lesssim x/h \lesssim 10$ it can be seen that the growth rates of the velocity fluctuation for flows with larger Wi are considerably smaller than that for the Newtonian jet [Fig. 4(a)]. Figure 3 also shows isolines of constant C_{ii}, indicating that structures of highly stretched polymers are organized as thin sheets that are nearly parallel and concentrated at the vicinity of the vortical sheets.

For both Newtonian and viscoelastic jets, at $x/h \lesssim 6.5$ the vorticity structures at the upper and lower shear-layers present oscillations that are approximately symmetric with respect to the flow centerline (Fig. 3 and videos at the Supplemental Material), indicating the dominance of the varicose shear-layer mode of instability at this region. This is not surprising since we are simulating cases where the inlet velocity profile is flat and the shear-layers are thin and is consistent with results from linear stability analysis of Newtonian [41] and viscoelastic [4] planar jets. Dominance of the shear-layer varicose mode at this initial region is typically observed in experiments involving short nozzles with high contraction ratios [42–45].

Antisymmetric undulations of the vorticity structures can be observed for the viscoelastic jet at Wi = 4 and $x/h \gtrsim 10$ (Fig. 3 and videos at the Supplemental Material), indicating that the sinuous jet column mode of instability is the dominant one at these farther locations, consistently with the experiments of Yamani *et al.* (2022) [7]. This shift from varicose to sinuous as the flow evolves downstream is associated with the evolution of the mean velocity profile, from nearly top-hat at the jet orifice to nearly parabolic downstream the end of the potential core. However, the sinuous undulations observed here are more pronounced for the viscoelastic jet than for the Newtonian jet, suggesting that the stabilizing effect of viscoelasticity at the nonlinear regime also contributes to the appearance of the sinuous instability. This result is the opposite of that obtained from temporal linear stability analysis of Oldroyd-B fluids at order unit elasticity (El $\sim$ 1) by Rallison and Hinch [2], who predicted that the sinuous mode is more stabilized than the varicose mode. Nevertheless, our result does not disproof their theoretical prediction, since here we are concerned with the more realistic case of low elasticity (El $\sim 10^{-4}$), and at $x/h \gtrsim 10$ the perturbation velocity is too large for any meaningful comparison with linear theory.

The $\|\boldsymbol{\omega}\|$ contours discussed above are useful for the analysis of the morphology of the vorticity structures, but they do not contain information about the direction of the vorticity vector. At the transitioning shear-layers, this can be obtained from the larger $\boldsymbol{\omega}$ component which is the spanwise vorticity ω_z. For the Newtonian jet, two-dimensional contours of ω_z do not add much to the description and merely show that $\boldsymbol{\omega}$ points at opposite directions at the lower and upper shear-layers [Fig. 5(a)]. However, a very peculiar distribution appears at the disturbed shear-layers of the viscoelastic jet at higher Wi [Fig. 5(b)]. In this case, it can be seen that at the upper shear-layer the larger vorticity sheets with positive ω_z (yellow) are surrounded by two additional sheets with negative ω_z (blue), forming a three-layered structure that is very thin and therefore is associated with intense vorticity gradients. The same is true for the lower shear-layer, but the signs of ω_z are reversed.

Since $\omega_z = \partial v/\partial x - \partial u/\partial y$ and on average $|\partial u/\partial y| \gg |\partial v/\partial x|$, the results reported above indicate that the profiles of $\partial u/\partial y$ will be very different for the viscoelastic jet at high Wi. The perturbations are very sensitive to the shape of the base flow $\bar{u}$ [39], and it is anticipated that this would have a large impact on their evolution.
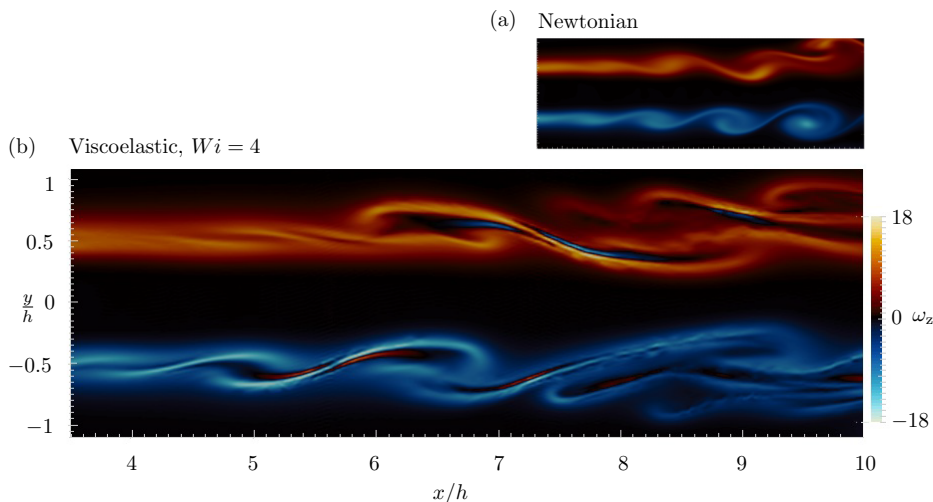
FIG. 5. Two-dimensional contours of instantaneous spanwise vorticity ω_z for Newtonian (a) and viscoelastic jet (b). The same region of the domain is shown in both cases, and a zoom is applied at the nonlinear region of the transitioning shear-layers for maximum clarity. Panel (b) is enlarged so that the very fine three-layered sheet structure of the viscoelastic shear-layer (absent in the Newtonian case) can be observed more clearly.

In order to verify this, we analyze the transverse profiles of normalized mean velocity difference $\bar{u}^+ = (\bar{u} - U_\infty)/(U_c - U_\infty)$ and their y derivatives for jets at different Wi, displayed in Fig. 6 for $x/h = 6$. At high Weissenberg numbers, Fig. 6 confirms that viscoelasticity causes a significant distortion of the mean velocity profile. For the Newtonian jet, a local minimum on the velocity derivative corresponding to an inflection point in the velocity profile is located at $y/\delta_{0.5} \approx 0.95$, where $\delta_{0.5} = \delta_{0.5}(x)$ is the half-width of the jet, defined in the classical way by $\bar{u}(x, y = \delta_{0.5}(x)) - U_\infty = 0.5[U_c(x) - U_\infty]$. It is known that this inflection point on the profile gives origin to the shear-layer instability [46]. For viscoelastic jets, the influence of increasing Wi is concentrated on the shear-layer $0.7 \lesssim y/\delta_{0.5} \lesssim 1.3$, where the absolute value of the velocity gradients are higher and thus the polymer chains are more stretched. For the viscoelastic jet at higher Wi a strong attenuation of the velocity gradient caused by viscoelasticity gives rise to two additional inflection points on the mean velocity profile that correspond to two new local minima, at $y/\delta_{0.5} \approx 0.78$ and $y/\delta_{0.5} \approx 1.23$, with the original inflection point at $y/\delta_{0.5} \approx 1$ becoming a local maximum velocity gradient. This is consistent with the double sheet structure that was observed at the lower and upper shear-layers,
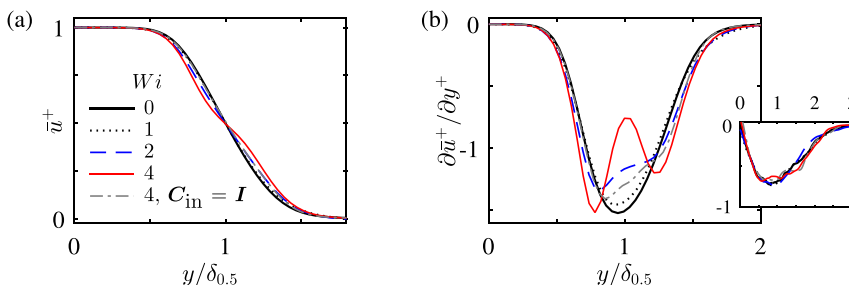

FIG. 6. Transverse profiles at $x/h = 6$: (a) normalized mean velocity and (b) normalized mean velocity derivative. $\bar{u}^+ = (\bar{u} - U_\infty)/(U_c - U_\infty)$ and $y^+ = y/\delta_{0.5}$. The inset in panel (b) shows $\partial\bar{u}^+/\partial y^+$ versus y^+ in the fully turbulent far-field, at $x/h = 16$.
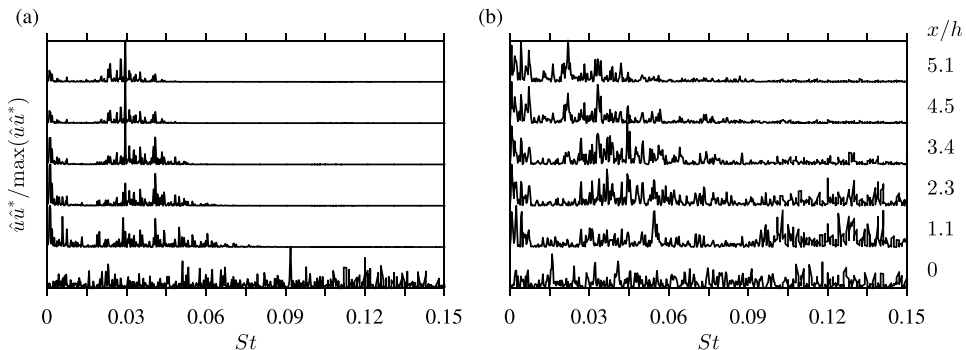
FIG. 7. Normalized spectra of perturbation energy at several x/h stations, $y/h = 0.5$ and $z/h = 0$ (middle plane): (a) Newtonian jet and (b) viscoelastic jet with Wi = 2.

when the vorticity contours were analyzed in Figs. 3(b) and 5(b), and will be crucial for the nonlinear stabilization mechanism proposed later in Sec. IV.

At the fully turbulent far-field, at $x/h \gtrsim 15$, $\bar{u}^+$ is very similar for Newtonian and viscoelastic jets [cf. inset of Fig. 6(b)], indicating enhanced flow divergence for viscoelastic jets, a topic that will be further investigated in Sec. III C. The attenuation of the velocity gradient caused by viscoelasticity is less intense for the DNS that uses the isotropic inlet condition for C (Fig. 6). This is so, because, at the near field, the polymers are less stretched when the isotropic inlet condition is used, especially at the shear-layer, resulting in a smaller back-reaction polymer force. For example, for Wi = 4, the jet that uses the Couette flow inlet condition for C has $\overline{C}_{ii}(x/h = 6, y/\delta_{0.5} = 1) \approx 700$, while the one that uses the isotropic inlet condition has $\overline{C}_{ii}(x/h = 6, y/\delta_{0.5} = 1) \approx 360$ (not shown).

B. Perturbation velocity in Fourier space

In order to analyze the growth of different instability modes in more detail we consider the temporal Fourier transform of streamwise velocity fluctuations $\hat{u}$ and its complex conjugate $\hat{u}^*$ at different locations of the flow. Several spectra of perturbation energy $\hat{u}\hat{u}^*$ are displayed in Fig. 7, plotted against the nondimensional frequency or Strouhal number St $= 2f\theta_0/(U_J + U_\infty)$. These were collected at the upper shear-layer $y/h = 0.5$, at the middle plane $z = 0$, and at five different x/h stations that correspond approximately to the linear region of instability growth of the Newtonian jet. At the inlet ($x = 0$) the spectra are very broad and the kinetic energy of perturbation is not concentrated in any particular mode, i.e., we have conditions that are characteristic of a natural jet without periodic forcing. For the Newtonian jet [Fig. 7(a)], all modes with St $\gtrsim 0.08$ have already decayed at $x/h = 1.1$ and analyzing the remaining spectra it is clear that the fastest growing mode is that associated with a Strouhal number of St ≈ 0.03, as a prominent peak appears for St ≈ 0.03 near the end of the linear region ($x/h = 4.5$). This value of the Strouhal number corresponds to the roll-up frequency of the Kelvin-Helmholtz instability and is a well-known result from linear stability theory and experiments [30–33].

Comparing Figs. 7(a) and 7(b) it can be seen that the polymers strongly influence the evolution of the spectrum of perturbation energy. The spectra are broader for the viscoelastic case and no distinctive single peak is observed as for the Newtonian case. In contrast, several peaks appear at different frequencies. Additionally, there are several viscoelastic modes with St > 0.08 that grow early on instead of immediately decaying as in the Newtonian jet. This destabilization of higher frequency modes (short waves) for flows at low El is in agreement with the earlier roll-up of the viscoelastic shear-layer, in comparison to the Newtonian case, that has been described in the paragraphs above. It has also been observed in experiments of a mixing-layer with polyethylene oxide (PEO) [47], DNS of temporally evolving mixing-layers of FENE-P flu-
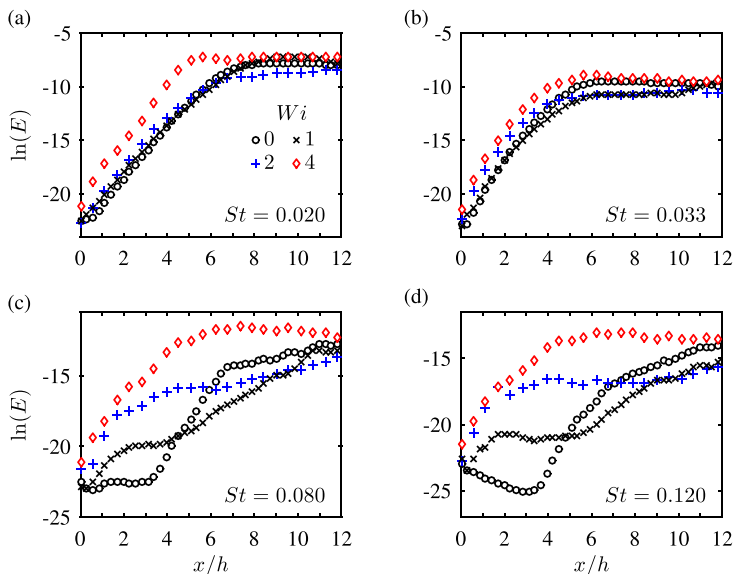
FIG. 8. Streamwise evolution of the logarithm of the normalized perturbation energy of disturbances associated with different Strouhal numbers.

ids [5], and by temporal dynamic mode decomposition analysis of experimental data of planar jets with PEO [7], even though these earlier works were conducted at more moderate Reynolds numbers.

A quantity that measures the perturbation kinetic energy contained in each instability mode, that is useful for analyzing their evolution, is given by

$$E(x; \text{St}) = \int_{-\infty}^{\infty} \frac{\hat{u}\hat{u}^*}{\theta_0 U_J^2} dy. \tag{10}$$

For spatially evolving two-dimensional disturbances with the form

$$\hat{u} = \phi(y) \exp[i(\alpha_r x - \beta_r t) - \alpha_i x], \tag{11}$$

where $\beta_r = 2\pi f$ is the angular frequency, α_r is the wave number, $i = \sqrt{-1}$ is the imaginary unit, and $\phi(y)$ is the amplitude of oscillation, simple algebraic manipulations show that the nondimensional growth rate $-\alpha_i \theta_0$ can be obtained from $E(x; \text{St})$ using the following formula [31,32,48]:

$$-\alpha_i \theta_0 = \frac{\theta_0}{2h} \frac{d[\ln(E)]}{d(x/h)}. \tag{12}$$

Equation (11) is a solution of the instability problem at the linear region, for both Newtonian [30–32,48] and viscoelastic fluids [1–5], but a formula similar to (12) has also been used to quantify the growth rate at the nonlinear region [49].

The streamwise evolution of $\ln E$ is shown in Fig. 8 for four instability modes that for a Newtonian shear-layer at the linear region correspond to a growing mode with $\text{St} = 0.020$, the fastest growing mode $\text{St} = 0.033$, the neutral mode $\text{St} = 0.080$, and a decaying or damped mode $\text{St} = 0.120$. For the Newtonian jet all modes show a linear region at $0.5 \lesssim x/h \lesssim 3.5$. The curve of the most unstable mode with $\text{St} = 0.033$ starts to bend at $x/h \approx 4.5$, where the shear-layer starts to roll up leading to a nonlinear evolution of perturbations and reaches a plateau at $x/h \approx 7$. In contrast, the viscoelastic cases at higher Wi reach the plateau of the perturbation energy earlier so that the
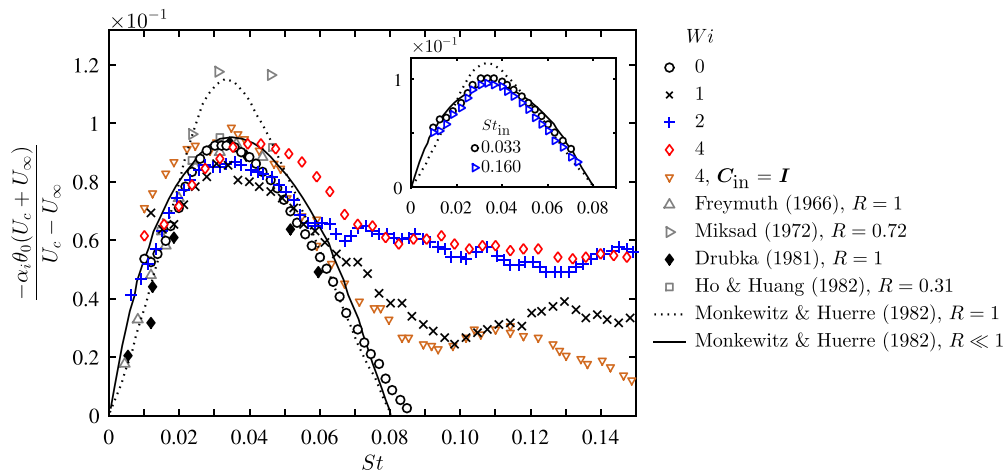
FIG. 9. Normalized growth rate of instabilities at the linear region for several instability modes. Some results from experiments and linear stability theory, from the literature, are also shown for comparison with the Newtonian case. The inset compares results from two Newtonian DNS that use different values of the inlet noise parameter St_{in}. $R = (U_c - U_\infty)/(U_c + U_\infty)$.

initial linear region is shorter. Additionally, at the linear region viscoelasticity clearly destabilizes the shorter waves with $\text{St} = 0.080$ and $\text{St} = 0.120$. However, at the nonlinear region ($4.5 \lesssim x/h \lesssim 12$) the viscoelastic curves with $\text{St} = 0.080$ and $\text{St} = 0.120$ grow slower than the Newtonian curves, showing now a stabilizing viscoelastic effect in agreement with the results discussed before.

We have calculated the slopes of the straight lines that best fit the $\ln E$ curves at $0.5 \lesssim x/h \lesssim 2.5$ and implemented formula (12) to calculate the values of the growth rates of several modes of instability at the linear region, similarly to previous experimental works of Newtonian shear-layers [31,32,48]. The results are displayed in Fig. 9, together with some data from experiments and linear stability analysis of the Newtonian shear-layer [31–33,50]. The adopted normalization is due to Monkewitz and Huerre [33] and brings the curves for shear-layers with large and small velocity differences to the same scale. For the Newtonian case, good agreement is obtained between our numerical results and those from experiments and linear theory.

The destabilizing effect of the polymers at the linear region is clear from Fig. 9. Destabilization occurs for shorter waves first (larger St) and as Wi is increased viscoelasticity contaminates modes with lower values of St until most of the modes become more unstable at the highest Wi in comparison to the Newtonian case. For example, at $\text{St} = 0.033$ we have $-\alpha_i \theta (U_c + U_\infty)/(U_c - U_\infty) = 0.093$ and 0.092 for $\text{Wi} = 0$ and 4, respectively. However, at $\text{St} = 0.08$, where the Newtonian growth rate is close to zero ($-\alpha_i \theta (U_c + U_\infty)/(U_c - U_\infty) = 0.009$), we obtain $-\alpha_i \theta (U_c + U_\infty)/(U_c - U_\infty) = 0.038$ for $\text{Wi} = 1$ and 0.061 for $\text{Wi} = 2$ and 4. Although the neutral mode of the Newtonian jet is at $\text{St} \approx 0.086$, those of viscoelastic jets with $\text{Wi} = 1$ and $\text{Wi} = 2$ or 4 are at much larger Strouhal numbers at $\text{St} \approx 0.22$ and $\text{St} \approx 0.35$, respectively (not shown). As mentioned earlier, these results are consistent with previous numerical and experimental works [5,7,47].

The viscoelastic destabilization is more intense for jets that use the Couette flow solution as the inlet condition for C, in comparison to the one that uses the isotropic inlet condition. As mentioned earlier, this is due to the different levels of polymer stretching that are obtained with the different inlet conditions.

The speed of propagation of the different instability modes, i.e., the wave speed or phase velocity C_{ph}, can be calculated from the downstream evolution of the phase angle distribution φ. First, the
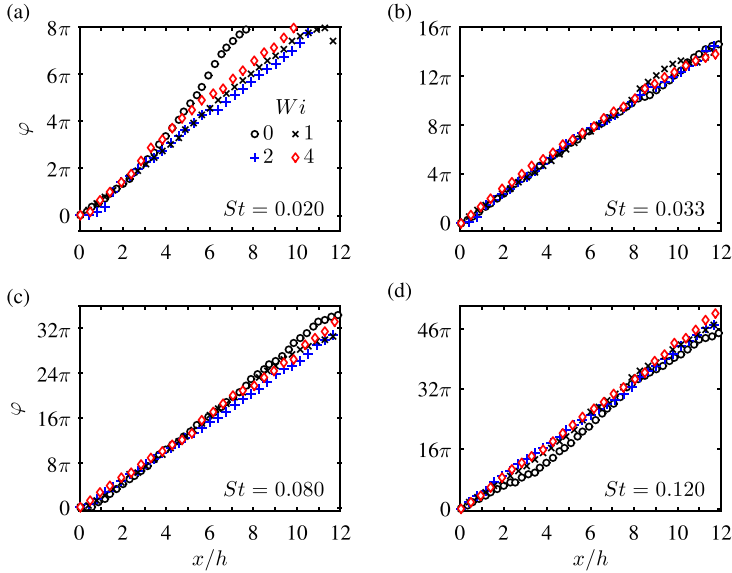
FIG. 10. Streamwise variation of the phase angle, at $y/h = 0.5$, for instabilities with different Strouhal numbers.

wave number is obtained using the following relation:

$$\alpha_r = \frac{\partial \varphi}{\partial x}, \tag{13}$$

where the phase angle is

$$\varphi = \arg(\hat{u}). \tag{14}$$

The phase velocity is by definition the ratio of the angular frequency and the wave number,

$$C_{\mathrm{ph}} = \frac{\beta_r}{\alpha_r}. \tag{15}$$

The argument of the complex perturbation velocity was calculated using the atan2 Fortran function, $\arg(\hat{u}) = \mathrm{atan2}(\hat{u}_I, \hat{u}_R)$, where $\hat{u}_I$ and $\hat{u}_R$ are the imaginary and real components of $\hat{u}$, respectively, i.e., $\hat{u} = \hat{u}_R + i\hat{u}_I$, and adding 2π radians for each full turn of the trigonometric circle [51]. When $\hat{u}_R$ is positive the atan2 function is just $\arctan(\hat{u}_I/\hat{u}_R)$, but the general definition is more involving and is able to calculate the correct quadrant of the trigonometric circle when $\hat{u}_R$ is nonpositive. Equation (13) follows from the local linear-instability solution (11), after rewriting it in polar coordinates and performing algebraic manipulations, and this approach has been adopted in experimental studies [31,32,42,49–53].

The streamwise evolution of φ at the shear-layer is shown at Fig. 10, for instabilities with four different values of St. A linear variation can be clearly identified, in agreement with linear stability theory. According to Eq. (13), the slope of the curves gives the wave number α_r, and they were obtained using linear interpolation at $2 \leqslant x/h \leqslant 4$. The phase velocities follow from Eq. (15), and the results are discussed below.

The values of C_{ph} obtained from our DNS are shown in Fig. 11, together with experimental results from the literature [31,32,42,50,52,53]. Comparison of C_{ph} with experimental data is a challenging test for a numerical simulation, and the good level of agreement displayed in Fig. 11 emphasizes the robustness of our DNS.
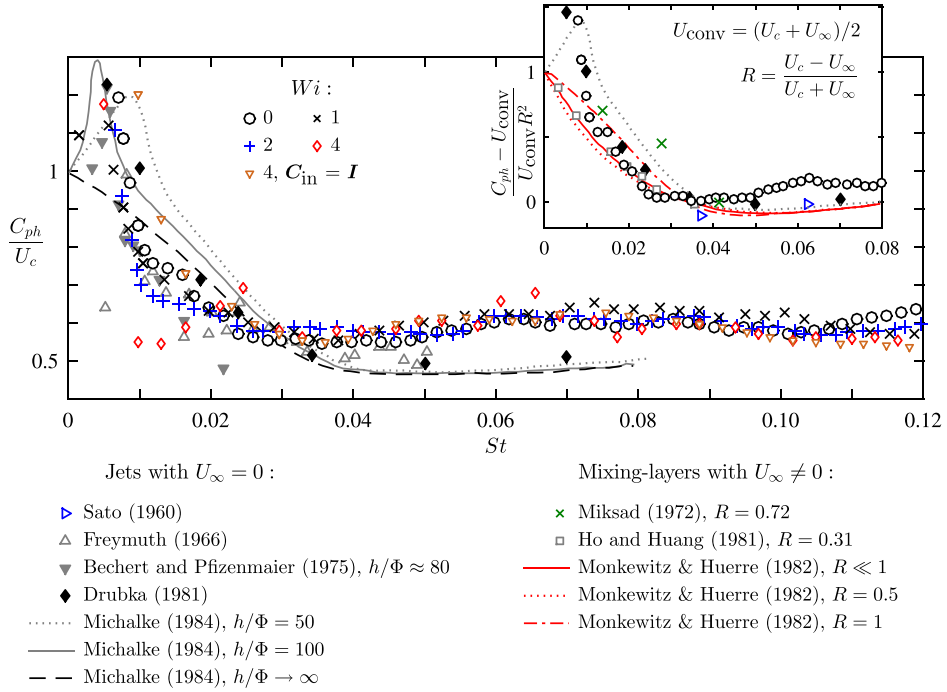
FIG. 11. Wave speeds (phase velocities) evaluated at $y/h = 0.5$ and normalized by centerline mean velocity of the jet. Experimental and theoretical results from the literature are also shown for comparison with the Newtonian DNS. The inset shows the data with the normalization proposed by Monkewitz and Huerre [33].

The phase velocity is particularly sensitive to the base flow parameters h/Φ and $R = (U_c - U_\infty)/(U_c + U_\infty)$, as demonstrated by linear stability analyses [33,39], whose results are also shown in Fig. 11. In fact, C_{ph} was predicted for the first time by Batchelor and Gill [38], using temporal linear stability analysis of a cylindrical vortex sheet, i.e., a plug flow with $\theta_0 = 0$. The theoretical result of Michalke [39], for spatially evolving disturbances to a hyperbolic-tangent profile with $h/\Phi \to \infty$, is similar to that obtained by Batchelor and Gill [38] and is displayed in Fig. 11. In that case, the long-waves limit of C_{ph} is equal to the centerline velocity of the jet, and monotonically decays towards the short-waves plateau at larger St, whose value depends on the amount of coflow [33]; $C_{ph}(\text{St} \gtrsim 0.03) = \bar{u}(x, y = \delta_{0.5}) \approx (U_c + U_\infty)/2$ and $y = \delta_{0.5}$ corresponds to a critical layer, where the phase velocity equals the local mean velocity. For thin shear-layers with large but finite h/Φ, C_{ph} initially increases, reaches a local maximum where $C_{ph} > U_c$, and then decreases towards the short-waves limit. Bechert and Pfizenmaier [52] used the term "ultrafast wave motion" to describe these perturbations, since they can travel faster than the maximum mean velocity of the flow. All these results from linear stability theory are consistent with the experimental and DNS data.

The phase velocities of viscoelastic jets at different values of Wi are also shown in Fig. 11. Remarkably, all profiles approximately collapse into the same curve when normalized by the centerline velocity. This indicates that C_{ph} is invariant with respect to the Weissenberg number, despite the very different growth rates of perturbations at different Wi.

A quantity that characterizes the instabilities at the nonlinear regime is the Strouhal number of the plane jet column mode St_δ, which is defined by

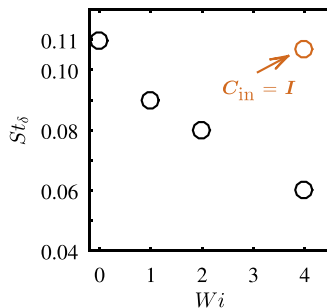$$\text{St}_\delta = \frac{f_p \delta_{0.5}}{U_c - U_\infty}, \tag{16}$$

FIG. 12. Strouhal number of the jet column mode at $x/h = 8.5$ and $y/\delta_{0.5} = 1$ as a function of the inlet Weissenberg number Wi.

where all quantities are evaluated at the shear-layer ($y/\delta_{0.5} = 1$), at the end of the potential core, i.e., at $x/h = 8.5$ and f_p is the corresponding peak frequency of the fluctuating velocity spectrum. St_δ corresponds to the nondimensional frequency of the passage of vortical structures at the end of the potential core and for Newtonian planar jets an approximately universal value exists [44,48,54–59], which is $St_\delta = 0.11 \pm 0.03$. This value compares well with the value calculated from our Newtonian DNS that is shown in Fig. 12. For viscoelastic jets St_δ is shown to decrease with the Weissenberg number, and we obtain $St_\delta = 0.06$ for the viscoelastic jet at the higher Weissenberg number (Wi = 4), corresponding to a reduction by a factor near two. This effect is much stronger when the inlet condition for the conformation tensor is the Couette flow solution: When the isotropic inlet condition is used, the reduction of St_δ is weak and $St_\delta = 0.107$ for Wi = 4.

C. Flow divergence

The locally parallel base flow assumption that has been adopted in linear stability analysis of Newtonian [33,39] and viscoelastic [1–4] free shear-layers requires that the changes in the base state are small over an instability wavelength. To test the accuracy of the assumption we calculate the wavelength distribution,

$$\lambda = \frac{2\pi}{\alpha_r}, \tag{17}$$

and plot transverse profiles of $\bar{u}$, their y derivatives, and the larger conformation tensor component $\overline{C_{xx}}$ at different values of $x/\lambda_{0.033}$, where $\lambda_{0.033}$ is the wavelength of the most unstable mode.

The λ/h distributions are shown at Fig. 13. The inset of Fig. 13 displays the normalized wave number $\alpha_r \theta_0$ obtained from our Newtonian DNS compared to experimental and theoretical results from the literature [31,51], merely to show that, for this quantity, good agreement is obtained. The wavelength of the most unstable mode, i.e., that with St = 0.033, is $\lambda_{0.033} = 1.65h$ for both Newtonian and viscoelastic jets. All modes with St $\geqslant 0.02$ have $\lambda < 3h$ and for these waves at least one instability wavelength is contained inside the linear region of perturbation growth. Modes with St $\lesssim 0.006$ have $\lambda > 18h$, i.e., their wavelengths are larger than the computational domain size $L_x = 18h$, a situation that would also be encountered in experiments due to the finite size of a wind tunnel or water tank. Nevertheless, our domain size validation study demonstrates that this does not have an influence on our results (cf. Appendix C).

Transverse profiles of $\bar{u}(x, y)/U_J$ and their y derivatives are shown in Figs. 14(a)–14(d), for both Newtonian and viscoelastic jet with Wi = 4, at five different stations within the potential core: $x/\lambda_{0.033} = 1, 2, 3, 4,$ and 5, corresponding to $x/h = 1.65, 3.3, 4.95, 6.6,$ and 8.25. For Newtonian jet at the linear region, the change of $\bar{u}(x, y)/U_J$ is small over one instability wavelength [Figs. 14(a) and 14(b)], which validates the local instability approximation. At the nonlinear region, more
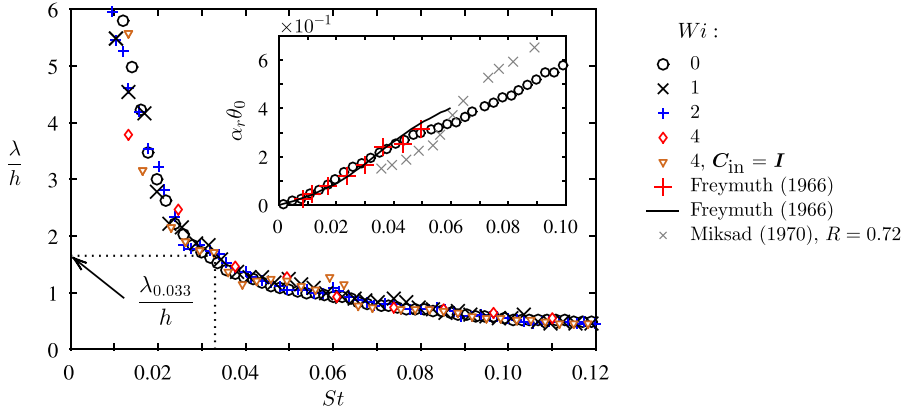
FIG. 13. Wavelength of instabilities at $y/h = 0.5$. The inset shows the wave-number distribution obtained from our Newtonian jet DNS compared with experimental and theoretical results from the literature.

pronounced changes are observed, which can be explained by the emergence of larger Reynolds stresses in that region (cf. Fig. 4).

In contrast, for the viscoelastic jet there are strong distortions of $\bar{u}(x, y)/U_J$ over one instability wavelength at both linear and nonlinear regions of perturbation growth (Figs. 14(c) and 14(d)]. The suppression of the velocity gradient at the shear-layer—and the appearance of additional inflection points on the base flow profile—is already visible at $x/\lambda_{0.033} = 2$. This effect is even larger at $x/\lambda_{0.033} = 3$ but starts loosing its intensity at downstream stations.
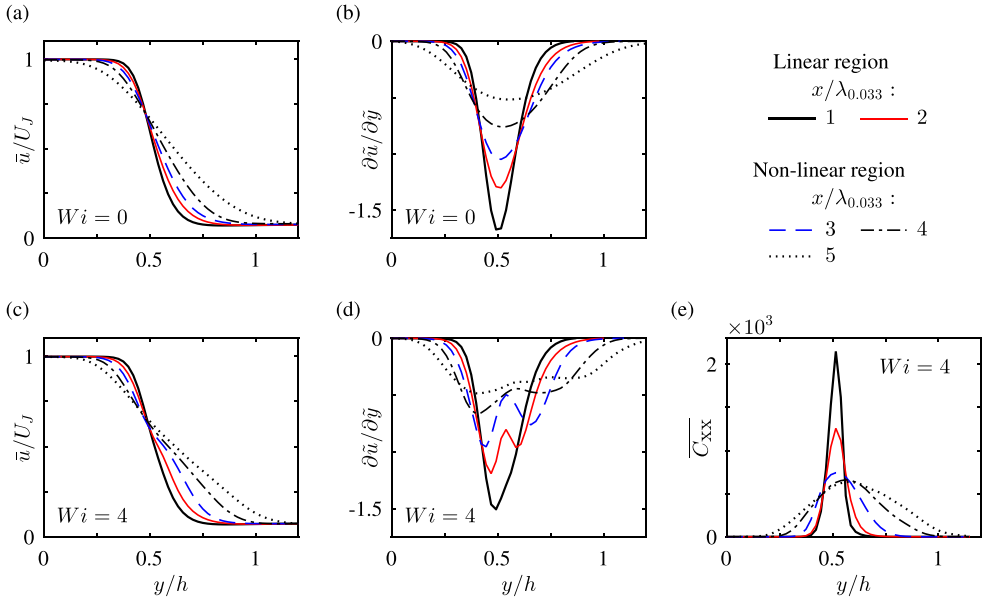

FIG. 14. Nondimensional transverse profiles of mean velocity [(a) and (c)], velocity derivative $\partial \tilde{u}/\partial \tilde{y} = (h/U_J)\partial \bar{u}/\partial y$ [(b) and (d)], and first normal component of the conformation tensor (e) at five different x stations within the potential core, for Newtonian and viscoelastic jet with Wi = 4.

At the linear region, the geometric shape of the transverse profile of $\overline{C_{xx}}$ does not change considerably, but its maximum value decreases by a significant amount over the distance of one instability wavelength, from max $\overline{C_{xx}} \approx 2149$ to 1258 at $x/\lambda_{0.033} = 1$ and 2, respectively, indicating that the polymers are predominantly relaxing in that region. However, the decay rate of max $\overline{C_{xx}}$ is much smaller downstream, e.g., max $\overline{C_{xx}} \approx 660$ and 637 at $x/\lambda_{0.033} = 4$ and 5, respectively. In contrast, at $x/\lambda_{0.033} = 3, 4$, and 5, and at y locations such as $y/h = 0.25$ and 0.75, there is actually a strong increase on the value of $\overline{C_{xx}}$ [Fig. 14(e)]. For example, at $y/h = 0.75$ we have $\overline{C_{xx}} = 68$, 275, and 440 at $x/\lambda_{0.033} = 3, 4$, and 5, respectively, which means that the polymers are stretching at these locations, instead of relaxing.

In summary, our results show strong flow divergence for viscoelastic jets at high Wi at both linear and nonlinear regimes of perturbation growth. Thus, the parallel base flow approximation that has been adopted in linear stability analysis of viscoelastic mixing-layers and jets [1–4] becomes less accurate as Wi is increased, and the inclusion of a nonparallel base flow as a refinement of those theories should be considered in the future.

For Newtonian jets, the effect of a slowly diverging base flow has been successfully incorporated into linear stability theories, using, e.g., multiple-scales analysis under the WKB approximation [60] and parabolized stability equations (Gudmundsson and Colonius [61] and references therein). These approaches ignore nonlinear intermodal interactions, but to some extent the effect of nonlinearities is implicitly captured by the changes of the base state $\bar{u}$, which is typically obtained from experimental measurements or DNS. Our DNS database of turbulent viscoelastic jets can be particularly useful in this framework, not only for providing reference results to compare the theory with but also because it can provide, in addition to $\bar{u}$, the components of the base-state conformation tensor $\overline{C_{ij}}$ and polymer stresses $\overline{\sigma_{ij}}^{[p]}$—quantities that presently cannot be experimentally measured in turbulent flows.

D. Jets with thick shear-layers: $h/\Phi = 5$

The instabilities of the jet are qualitatively different depending on the shape of the base flow profile. This was shown by Batchelor and Gill [38], who demonstrated using linear analysis of temporally evolving perturbations that round jets with thick shear-layers can only amplify anti-symmetrical disturbances—termed sinuous instabilities due to an earlier study by Lord Rayleigh [46]—in contrast to the symmetrical or varicose instability of thin shear-layer jets discussed in previous sections. Additionally, the spatiotemporal stability analysis of Ray and Zaki [4] revealed that viscoelastic effects are substantially weaker when the shear-layers are thick. In order to verify and complement these previous theoretical results, we performed jet DNS at $h/\Phi = 5$, i.e., jets with thick shear-layers (cf. Fig. 2). This section is devoted to these results, focusing on the characteristics that differ from the thin shear-layer results that were discussed in previous sections.

Two-dimensional contours of instantaneous vorticity magnitude are displayed in Fig. 15 for both Newtonian and viscoelastic jet at Wi = 8. The upper and lower vorticity sheets are approximately parallel to the flow direction up to $x/h \approx 15$, indicating a much lengthier linear region in comparison to that of thin shear-layer jets. Not surprisingly, these vorticity sheets are much thicker than those of thin shear-layers. For both Newtonian and viscoelastic jets, antisymmetrical undulations of the upper and lower vorticity sheets can be observed at $15 \lesssim x/h \lesssim 25$, confirming that the sinuous mode of instability is the dominant one for thick shear-layer jets. Additionally, the double vortex sheet structure observed earlier for the thin shear-layer jet at Wi = 4 [Fig. 3(b)] is absent for the viscoelastic thick shear-layer jet [Fig. 15(b)], despite the higher value of Wi of the latter, demonstrating that viscoelastic effects at the transition region are weaker for thick shear-layer jets. These observations are consistent with linear stability analyses [4,38]. The addition of polymers appears to have a larger influence on the flow structures predominantly at the fully turbulent region, at $x/h \gtrsim 30$, where a depletion of small-scale eddies is observed.

The streamwise evolution of the normalized perturbation and mean components of velocity are shown in Fig. 16. At the linear region of perturbation growth, displayed in the inset of Fig. 16(a),
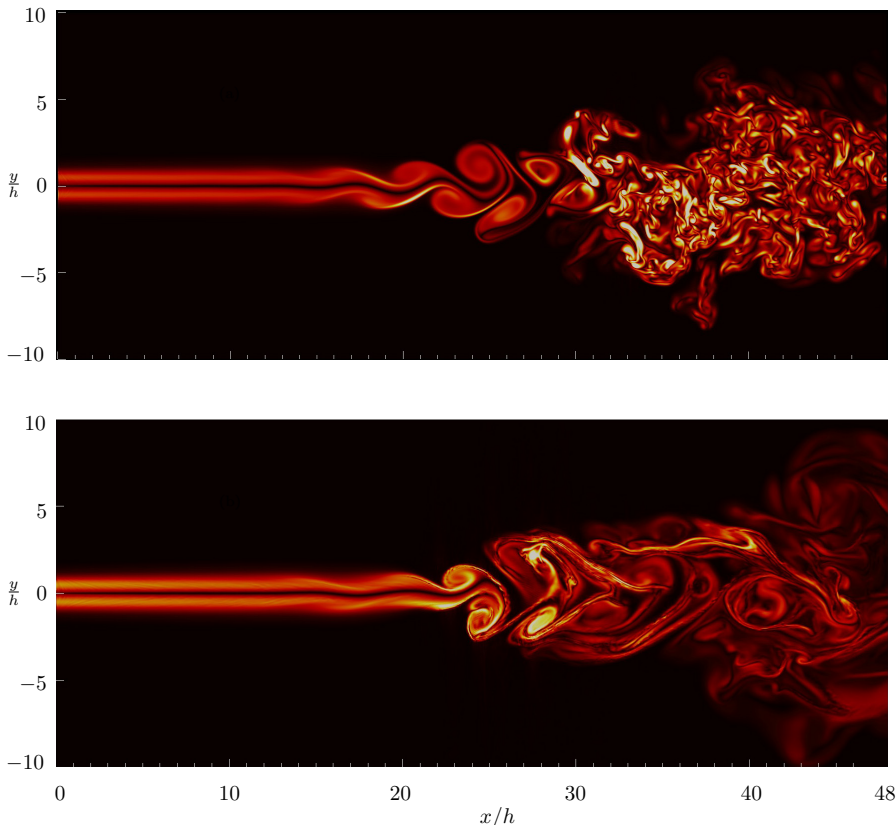
FIG. 15. Two-dimensional contours of instantaneous vorticity magnitude at the middle plane ($z/h = 0$) for (a) Newtonian and (b) viscoelastic jet with Wi = 8. Both jets have thick shear-layers at the inlet, with $h/\Phi = 5$, and the sinuous mode of instability is observed.

destabilization is promoted by viscoelasticity only for the jet with Wi = 8, and at the nonlinear regime at $15 \lesssim x/h \lesssim 25$ the perturbation velocities of the Newtonian and viscoelastic jets are nearly indistinguishable. This is in contrast with the results reported earlier for thin shear-layer jets and attest that the influence of the polymers on the instabilities is much weaker for thick shear-layer jets.

In the fully turbulent region at $x/h \gtrsim 25$, however, a different picture is observed and increasing Wi leads to a suppression of the normalized perturbation velocity [Fig. 16(a)] and a decrease of the decay rate of the centerline mean velocity [Fig. 16(b)].

The striking differences between thin and thick shear-layer viscoelastic jets at the transition region can be explained by the different levels of polymer stretching that exist for the two cases, that results from the different levels of deformation rates imposed by the inlet velocity gradients. For thick shear-layers, the mean component of the velocity gradient is not large enough to promote the stretching of polymers at the shear-layer, and the fluctuating component is only significant at the late stages of transition and at the fully turbulent region. For thin shear-layers, on the other hand, the mean velocity gradient is substantially larger (cf. Fig. 2) and stretches the polymers considerably.

This is confirmed in Fig. 17, which shows two-dimensional contours of the instantaneous trace of the conformation tensor for both thick and thin shear-layer jets. In both cases, thin sheets of highly stretched polymers can be observed, but only at $x/h \gtrsim 25$ for thick shear-layers, which in this case are triggered by the emergence of turbulent deformation rates at this region. For the thin
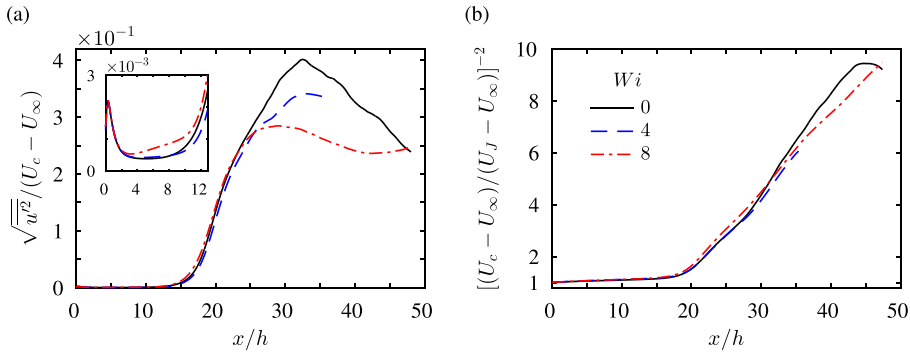
FIG. 16. Streamwise evolution of normalized rms velocity along the centerline (a) and centerline mean velocity difference (b) for jets with thick shear-layers ($h/\Phi = 5$). The inset in panel (a) shows a zoom at $0 \leqslant x/h \leqslant 12.5$.

shear-layer jet, the polymers are highly stretched not only at the fully turbulent far-field but also at the transitioning shear-layers, since there the mean velocity gradients are large enough.

These results indicate that the definition of the Weissenberg number that more accurately quantifies the viscoelastic influence on the transition of jets and mixing-layers is one that is
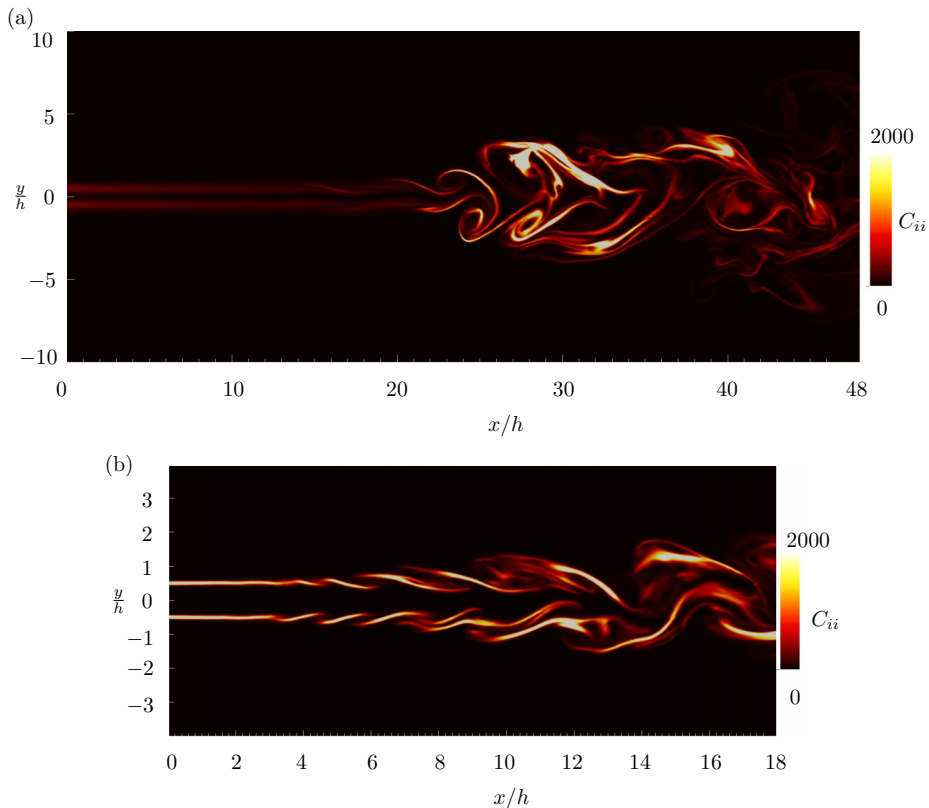

FIG. 17. Two-dimensional contours of the trace of the instantaneous conformation tensor at the middle plane ($z/h = 0$) for (a) viscoelastic jet with thick shear-layers at the inlet ($h/\Phi = 5$) and Wi = 8 and (b) viscoelastic jet with thin shear-layers at the inlet ($h/\Phi = 40$) and Wi = 4.
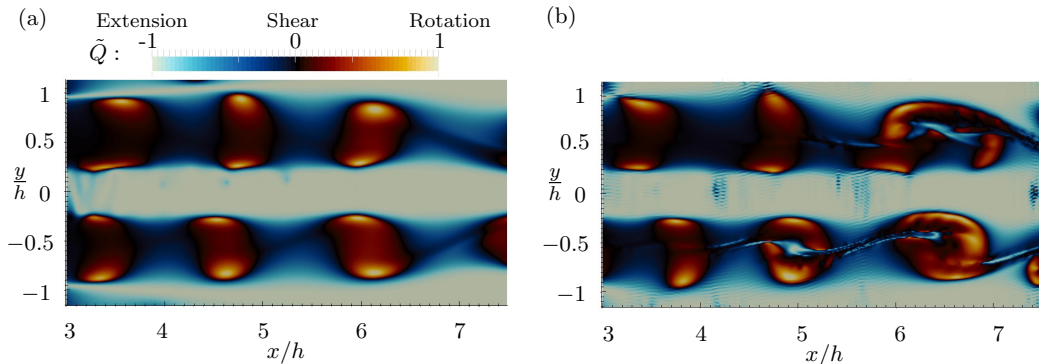
FIG. 18. Two-dimensional contours of the flow instantaneous classification parameter $\tilde{Q}$ for Newtonian (a) and viscoelastic jet with Wi = 4 (b) and thin shear-layers ($h/\Phi = 40$).

based on the actual mean velocity gradient at the inlet, instead of the velocity difference, i.e., $\mathrm{Wi}_{\partial u} = \tau_p \max|\partial \bar{u}/\partial y|$. Using this definition for the cases with Wi = 4, we have $\mathrm{Wi}_{\partial u} \approx 40$ and 3.75 for thin and thick shear-layer jets at $h/\Phi = 40$ and 5, respectively, i.e., the thin shear-layer jet has a $\mathrm{Wi}_{\partial u}$ that is one order of magnitude larger, despite the same value of Wi.

IV. PHYSICAL MECHANISMS

This section discusses the physical mechanisms that are involved in the destabilization and stabilization promoted by the polymers at the different regimes of perturbation growth. First, we identify the flow kinematics in the jet configuration using a flow classification criterion in Sec. IV A. The physical mechanisms are discussed in Sec. IV B, where we analyze the interactions between polymers and flow from an energetic viewpoint. Finally, Sec. IV C investigates whether the concept of tensioned streamlines can be useful to explain the observed behavior.

A. Flow kinematics

Viscoelastic fluids behave differently depending on the flow kinematics and therefore it is important to identify which regions of the flow are dominated by shear, extensional, or rotational motions [62]. Here we adopt a flow classification criterion based on the flow parameter $\tilde{Q}$, defined by

$$\tilde{Q} = \frac{||\boldsymbol{W}||^2 - ||\boldsymbol{S}||^2}{||\boldsymbol{W}||^2 + ||\boldsymbol{S}||^2}, \tag{18}$$

where $\boldsymbol{W} = (\nabla \boldsymbol{u} - \nabla \boldsymbol{u}^T)/2$ and $\boldsymbol{S} = (\nabla \boldsymbol{u} + \nabla \boldsymbol{u}^T)/2$ are the vorticity and rate of strain tensors, respectively, and the Euclidean norm of a second-order tensor $\boldsymbol{A}$ is $||\boldsymbol{A}|| = \sqrt{\mathrm{tr}(\boldsymbol{A} \cdot \boldsymbol{A}^T)}$. This is similar to the Q criterion proposed by Hunt *et al.* [63] for vortex identification but with a normalization that has been adopted for flow classification. Values in the range $-1 \leqslant \tilde{Q} < 0$ represent regions dominated by extension, whereas $0 < \tilde{Q} \leqslant 1$ represents rotational regions and $\tilde{Q} = 0$ represents regions that are shear-dominated. These regions are also termed hyperbolic, elliptical, and parabolic, respectively.

Two-dimensional contours of instantaneous $\tilde{Q}$ are shown in Fig. 18, where for clarity a zoom is applied in the region given by $3 \leqslant x/h \leqslant 7.5$ and $-1.15 \leqslant y/h \leqslant 1.15$. Near the jet centerline, at $-0.2 \lesssim y/h \lesssim 0.2$, and at the free-stream regions, at $y/h \gtrsim 1$ and $y/h \lesssim -1$, the flow is extensional. However, at the upper and lower shear-layers, at $0.2 \lesssim y/h \lesssim 1$ and $-1 \lesssim y/h \lesssim -0.2$, respectively, the flow is more complex and presents mixed kinematics, containing a combination of rotation, shear, and extension. Spanwise rollers can be clearly observed, and these rollers are

connected by shear-dominated strips that are oriented on the direction of the maximum mean shear. For the viscoelastic jet, we verified by a comparison with two-dimensional contours of C_{ii}, similar to those displayed at Fig. 17(b), that the polymers are considerably stretched nearby the shear-dominated strips, and Fig. 18(b) shows that this is associated with distortions of the flow parameter $\tilde{Q}$ on their periphery, where extension-dominated regions also appear. These distortions can also be observed at the centers of some spanwise rollers.

B. Energy transfers between polymers and flow field

The analysis in Sec. III has shown that in the linear region the polymers are predominately relaxing [Fig. 14(e)], the perturbation velocity amplifies and the mean velocity neither grows nor decays (Fig. 4) and is merely distorted by the action of the polymers. This suggests the following mechanism for the viscoelastic destabilization that is obtained when Wi is increased: The relaxing polymers release their potential elastic energy, which is partially absorbed by the perturbations, increasing their kinetic energy.

In order to verify this hypothesis, we perform an inspection of all terms of the evolution equation of the total perturbation kinetic energy $\bar{q} = (\overline{u'^2} + \overline{v'^2} + \overline{w'^2})/2$:

$$\bar{\boldsymbol{u}} \cdot \nabla \bar{q} = -\frac{1}{\rho} \nabla \cdot \overline{p'\boldsymbol{u}'} - \frac{1}{2} \nabla \cdot \overline{\boldsymbol{u}'\boldsymbol{u}' \cdot \boldsymbol{u}'} + \nu^{[s]} \nabla^2 \bar{q} - \overline{\boldsymbol{u}'\boldsymbol{u}'} : \nabla \bar{\boldsymbol{u}} - \varepsilon^{[s]}$$
$$+ \frac{1}{\rho} \nabla \cdot \overline{\boldsymbol{\sigma}'^{[p]} \cdot \boldsymbol{u}'} - \frac{1}{\rho} \overline{\boldsymbol{\sigma}'^{[p]} : \nabla \boldsymbol{u}'}. \tag{19}$$

The last two terms on the right-hand side of Eq. (19) represent fluxes of energy between the perturbations and the polymers and can be positive or negative depending on whether the perturbations are absorbing from or releasing energy to the polymers, respectively. Transverse profiles of all terms of Eq. (19) at $x/h = 3$ are shown in Figs. 19(a) and 19(b). For the viscoelastic jet, $\nabla \cdot \overline{\boldsymbol{\sigma}'^{[p]} \cdot \boldsymbol{u}'}/\rho - \overline{\boldsymbol{\sigma}'^{[p]} : \nabla \boldsymbol{u}'}/\rho$ is the largest and therefore dominant term of the equation, and it is positive everywhere, confirming that the relaxing polymers destabilize the flow by transferring part of their energy to the perturbations.

The budgets of perturbation kinetic energy are also useful to elucidate the mechanism of viscoelastic stabilization at the nonlinear region. In this region, the polymers are still relaxing at the middle of the shear-layer, albeit at a much smaller rate than upstream, but are stretching considerably on its periphery, as shown by Fig. 14(e) described earlier. It is tempting to think that the polymers in these regions stretch by absorbing the kinetic energy of the perturbations, therefore stabilizing the flow. However, our results revealed that this is not the case, and the actual mechanism involves an indirect action of the polymers on perturbations, discussed below.

As the perturbations travel in the flow direction and enter the nonlinear region, the maximum value of $\overline{C_{ii}}$ becomes progressively smaller [Fig. 14(e)], whereas the Reynolds stresses become progressively larger [Fig. 4(a)] until the production of perturbation by the mean flow, the term $-\overline{\boldsymbol{u}'\boldsymbol{u}'} : \nabla \bar{\boldsymbol{u}}$ of Eq. (19), surpasses the viscoelastic flux and assumes the role of the dominant production term [Fig. 19(d)]. However, the polymers action on the mean flow causes a significant distortion of the base flow, resulting in a suppression of the mean velocity gradient $\nabla \bar{\boldsymbol{u}}$ (Fig. 6) that leads to a reduction of $-\overline{\boldsymbol{u}'\boldsymbol{u}'} : \nabla \bar{\boldsymbol{u}}$. Since $-\overline{\boldsymbol{u}'\boldsymbol{u}'} : \nabla \bar{\boldsymbol{u}}$ is now the dominant production term, the suppression of $\nabla \bar{\boldsymbol{u}}$ causes stabilization of the perturbations, resulting in smaller Reynolds stresses $\overline{\boldsymbol{u}'\boldsymbol{u}'}$ and therefore this stabilization mechanism is self-enhancing. Thus, at the nonlinear region, the polymers act indirectly on the perturbations, furnishing stabilization by a distortion of the mean flow field.

Figure 19(d) also shows that in the nonlinear region the viscoelastic flux $\nabla \cdot \overline{\boldsymbol{\sigma}'^{[p]} \cdot \boldsymbol{u}'}/\rho - \overline{\boldsymbol{\sigma}'^{[p]} : \nabla \boldsymbol{u}'}/\rho$ is actually destabilizing, since it is positive everywhere. Thus, there are two competing processes at play: (i) a direct one that destabilizes the flow through transfer of energy from the polymers directly to the perturbations and (ii) an indirect one that stabilizes the flow by a
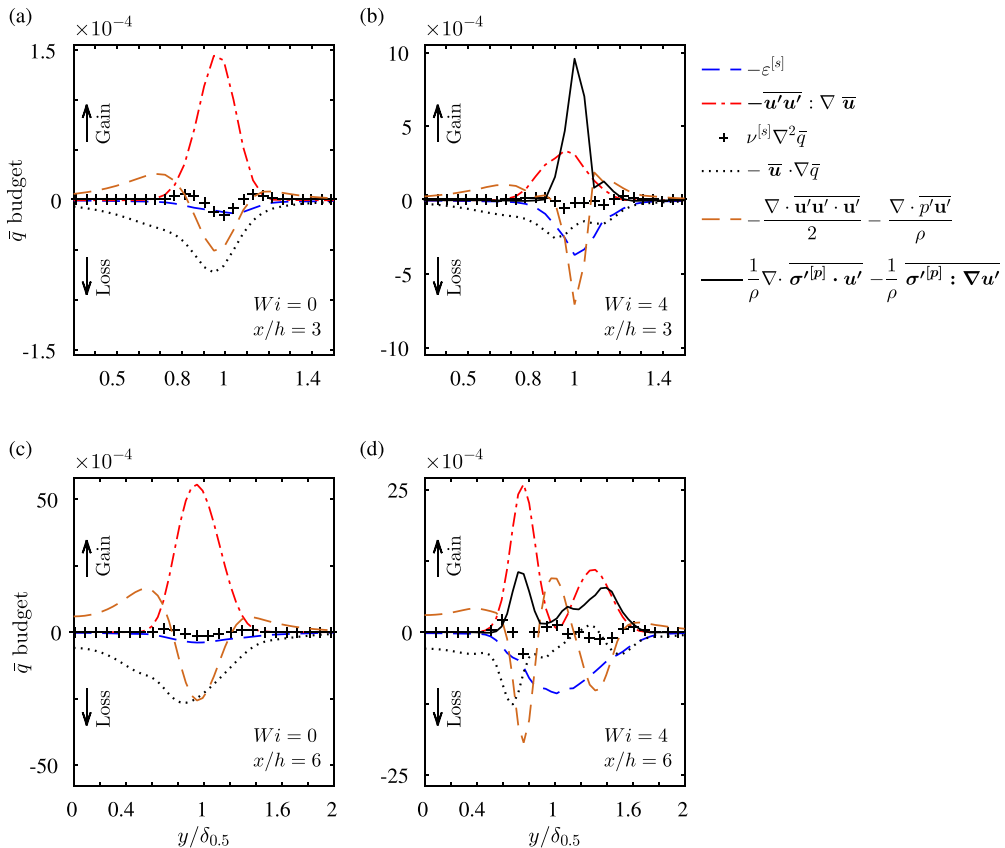
FIG. 19. Transverse profiles of the terms appearing in the balance equation of the total perturbation kinetic energy [Eq. (19)] at two x/h stations, within the linear [(a) and (b)], and nonlinear [(c) and (d)] regions of perturbation growth. All terms have been normalized by $U_c^3/\delta_{0.5}$. Notice the different scales used at the ordinates and abscissas of the plots.

distortion of the base state $\bar{u}$ that leads to a suppression of the production of turbulent energy. Overall stabilization or destabilization depends on which process is the dominant one. At the linear region, the perturbation velocities and Reynolds stresses are too small, and the direct polymer destabilization (i) dominates. At the nonlinear region, the perturbations become much larger and the indirect stabilization by a distortion of the base state (ii) is the dominant mechanism.

C. Polymer normal stresses along perturbed streamlines

The concept of tensioned streamlines has been widely used to explain a variety of viscoelastic flow phenomena. For example, when the mean-flow streamlines are curved the polymers introduce hoop stresses that lead to the rod-climbing effect [64] and to purely elastic instabilities at low Reynolds numbers [62,65,66]. The base-state streamlines of planar jets are predominately straight, except at a small portion of the irrotational region due to fluid entrainment. However, the instantaneous (perturbed) three-dimensional streamlines develop curvature at the shear-layer by the action of transverse perturbations, which becomes significant at the nonlinear regime of transition [Fig. 20(a)].

This section analyzes whether the polymer normal stresses along perturbed streamlines play a role on the linear destabilization or nonlinear stabilization mechanisms discussed in Sec. III.
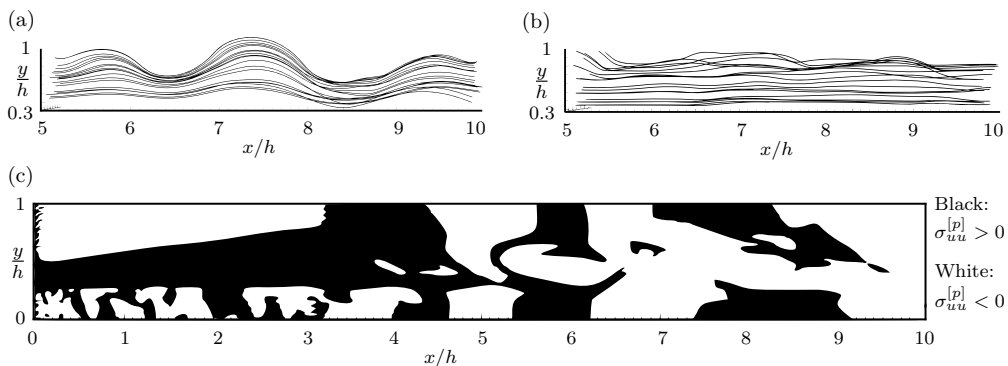
FIG. 20. Three-dimensional instantaneous streamlines at the nonlinear upper shear-layer region of (a) Newtonian jet and (b) viscoelastic jet with Wi = 4. (c) Two-dimensional contours of first normal polymer stress component along instantaneous streamlines, indicating the regions with polymer tension ($\sigma_{uu}^{[p]} > 0$) and compression ($\sigma_{uu}^{[p]} < 0$) along streamlines. Only the upper part of the jet is shown and as before the centerline is located at $y/h = 0$.

The first normal component of the polymer stress tensor projected along the direction of the instantaneous streamlines, $\sigma_{uu}^{[p]}$, is calculated using the following expression:

$$\sigma_{uu}^{[p]} = \boldsymbol{e}^T \cdot \boldsymbol{\sigma}^{[p]} \cdot \boldsymbol{e}, \tag{20}$$

where $\boldsymbol{e}$ is the unitary vector that is everywhere tangent to the streamlines $\boldsymbol{e} = (1/||\boldsymbol{u}||)\boldsymbol{u}$ ($||\boldsymbol{u}||$ is the Euclidean norm of $\boldsymbol{u}$), written in column matrix notation and $\boldsymbol{e}^T$ is its transpose.

At the nonlinear regime, the perturbed streamlines of the viscoelastic jet with Wi = 4 are considerably straighter in comparison to the Newtonian jet streamlines [Fig. 20(a) and 20(b)]. This is a consequence of the stabilizing effect of the polymers at the nonlinear regime, and possible reasons for that are (i) extra polymer tension along streamlines ($\sigma_{uu}^{[p]} > 0$) that increase their resistance to transverse deformations imposed by the perturbations, (ii) weaker perturbations in the viscoelastic case compared to the Newtonian case, and (iii) a combination of (i) and (ii). However, possibilities (i) and (iii) are ruled out when we analyze the two-dimensional contours of $\sigma_{uu}^{[p]}$, shown at Fig. 20(c). In the nonlinear region, at $x/h \gtrsim 5$, the polymers impose both tractive ($\sigma_{uu}^{[p]} > 0$) and compressive ($\sigma_{uu}^{[p]} < 0$) stresses, and at the nonlinear shear-layer there is a predominance of polymer compression instead of tension.

These results indicate that the dominant mechanism for viscoelastic stabilization at the nonlinear regime does not involve the concept of extra tension along perturbed streamlines. The suppression of the production term of velocity perturbation resulting from the distortion of the base state discussed in Sec. IV B seems to be the dominant mechanism at the nonlinear region.

On the other hand, at the linear region of perturbation growth the shear-layer is dominated by the presence of polymer tension along streamlines [$\sigma_{uu}^{[p]} > 0$, see Fig. 20(c) at $x/h \lesssim 4$ and $0.4 \lesssim y/h \lesssim 0.6$], and this is one of the ingredients of the mechanism for viscoelastic destabilization proposed by Page and Zaki [67], based on nonmodal linear stability analysis, where polymer tension along mean-flow streamlines provide support for the propagation of amplified vorticity waves.

V. CONCLUSIONS

Highly accurate direct numerical simulations (DNS) of spatially evolving submerged jets with viscoelastic FENE-P fluids at high Reynolds numbers were performed in order to study the influence of viscoelasticity on the evolution of the perturbations at the linear and nonlinear regimes of perturbation growth.

At the linear regime viscoelasticity is destabilizing; shorter waves destabilize first and as the Weissenberg number Wi is increased this effect propagates towards longer waves until most modes become more unstable. The frequency domain of instability of the viscoelastic jet at the highest Wi extends up to a Strouhal number of St ≈ 0.35, which is much larger than St ≈ 0.08 of the Newtonian jet.

In contrast, at the nonlinear regime viscoelasticity is stabilizing; the polymers attenuate the velocity gradients at the shear-layer region originating additional inflection points on the base flow velocity profile and a resultant double-sheet vortical structure that does not roll-up according to the Newtonian Kelvin-Helmholtz mechanism. This is accompanied by lower growth rates of fluctuating velocity at the nonlinear region and by a decrease of the nondimensional passage frequency of vortices by a factor of 1.8 for the case with the highest Wi. This dual character of the polymers, i.e., destabilizing or stabilizing at different regimes, has been documented in recent experimental studies of round and planar jets with polyethylene oxide [6,7] and illustrates the rich dynamics of polymer solutions.

Two competing instability mechanisms have been identified and analyzed to explain the observed results. The first one is destabilizing and involves a direct transfer of elastic energy from the relaxing polymers to the kinetic energy of perturbations. The second mechanism is an indirect one, where the polymers promote flow stabilization by causing a distortion of the base-state mean velocity profile that reduces the production of perturbation energy by the mean flow. Overall flow stabilization or destabilization depends on which mechanism is the dominant one at each regime; at the linear regime the former dominates, whereas the latter is dominant at the nonlinear regime.

Viscoelastic jet destabilization at the linear regime has been predicted by spatiotemporal local linear analysis [4], but a theory that considers nonlinearities of the perturbation equation of the viscoelastic jet is still lacking. Our results suggest that for thin shear-layers it is more adequate to include nonparallel base flow effects in the analysis, since strong flow divergence has been observed both at the linear and nonlinear regions of transition.

APPENDIX A: LATERAL AND OUTFLOW BOUNDARY CONDITIONS

This Appendix discusses the details of the boundary conditions used at the outlet boundary of the domain and at the boundaries facing the transverse and spanwise directions.

As mentioned in Sec. II B, periodic boundary conditions are imposed on the y and z directions. For the boundaries facing the vertical direction they are

$$\boldsymbol{u}(x, y = -L_y/2, z, t) = \boldsymbol{u}(x, y = L_y/2, z, t),$$
$$\boldsymbol{C}(x, y = -L_y/2, z, t) = \boldsymbol{C}(x, y = L_y/2, z, t), \tag{A1}$$

while for the boundaries facing the spanwise direction the conditions are given by

$$\boldsymbol{u}(x, y, z = -L_z/2, t) = \boldsymbol{u}(x, y, z = L_z/2, t),$$
$$\boldsymbol{C}(x, y, z = -L_z/2, t) = \boldsymbol{C}(x, y, z = L_z/2, t). \tag{A2}$$

A nonreflective outflow condition is used at the outlet boundary [27]. The starting point is the following equation:

$$\frac{\partial u}{\partial t} = -C_u(y,z,t)\frac{\partial u}{\partial x} - v\frac{\partial u}{\partial y} - w\frac{\partial u}{\partial z} + \nu^{[s]}\left(\frac{\partial^2}{\partial y^2} + \frac{\partial^2}{\partial z^2}\right)u + \frac{\partial\sigma_{xy}^{[p]}}{\partial y} + \frac{\partial\sigma_{xz}^{[p]}}{\partial z}, \qquad (A3)$$

which is similar to the x direction momentum equation except that the streamwise diffusion, polymer, and pressure gradient terms are absent and the convective velocity $C_u = C_u(y,z,t)$ appears in place of u for one of the inertial terms. Equation (A3) is evaluated at the plane located upstream the outlet plane, to obtain C_u, and the result is extrapolated to the outlet plane. The streamwise derivative is calculated with a first-order backward differencing scheme, and the y and z directions are treated with pseudospectral methods, for velocity, and second-order central finite differences, for the polymer stresses. We also define the maximum and minimum values that C_u is allowed to have in order to avoid convection velocities that are too large or too small [27]. They are $C_{u,\min} = 0.25[u(x = n_x - 2, y, z, t) + u(x = n_x - 1, y, z, t)]/2$ and $C_{u,\max} = 0.75[u(x = n_x - 2, y, z, t) + u(x = n_x - 1, y, z, t)]/2$. Finally, after the calculation of the local values of $C_u(y,z,t)$, Eq. (A3) is evaluated at the outlet plane, and advanced on time using the same third-order low-storage Runge-Kutta scheme adopted for Eqs. (1) and (3). No special treatment is given for the transverse and spanwise components of the velocity at the outlet boundary.

This nonreflective outflow condition guarantees that the vortical structures leave the computational domain without distortions. This was already shown in previous works [68,69] and can also be observed here in Figs. 3 and 15. When reflective outflow conditions are used instead of nonreflective ones used here, there is considerable accumulation of enstrophy (vorticity norm) at the outlet boundary, as demonstrated by Craske and van Reeuwijk (see Fig. 1 of their paper) [70], which can cause the loss of numerical stability of the simulation. This effect is clearly absent in our simulations.

The advection term of the conformation tensor equation is calculated with the Kurganov-Tadmor scheme [26], which requires special treatment at the outlet boundary in order to avoid terms that are not available in the computational grid, e.g., to avoid terms at $x = L_x + \Delta x$. Nearby the outlet boundary, special care is taken in the calculation of the conformation tensor $\boldsymbol{C}_{i,j,k}^{\pm}$, where the superscripts $\pm$ represent its limiting values at a given point (with indexes i, j and k) when approached from the right $(+)$ or from the left $(-)$. The calculations are carried out according to the following expressions:

$$\boldsymbol{C}_{n_x+1/2,j,k}^{+} = \boldsymbol{C}_{n_x,j,k}, \qquad (A4)$$

$$\boldsymbol{C}_{n_x+1/2,j,k}^{-} = \boldsymbol{C}_{n_x,j,k}, \qquad (A5)$$

$$\boldsymbol{C}_{n_x-1/2,j,k}^{+} = \boldsymbol{C}_{n_x,j,k}, \qquad (A6)$$

$$\boldsymbol{C}_{n_x-1/2,j,k}^{-} = \boldsymbol{C}_{n_{x-1},j,k}, \qquad (A7)$$

for the control volumes centered at the outlet boundary corresponding to $x = L_x$ and by

$$\boldsymbol{C}_{n_x-1+1/2,j,k}^{+} = \boldsymbol{C}_{n_x,j,k}, \qquad (A8)$$

$$\boldsymbol{C}_{n_x-1+1/2,j,k}^{-} = \boldsymbol{C}_{n_x-1,j,k} + \frac{\Delta x}{2}\left(\frac{\partial\boldsymbol{C}}{\partial x}\right)_{n_x-1,j,k}, \qquad (A9)$$

$$\boldsymbol{C}_{n_x-1/2,j,k}^{+} = \boldsymbol{C}_{n_x,j,k} - \frac{\Delta x}{2}\left(\frac{\partial\boldsymbol{C}}{\partial x}\right)_{n_x,j,k}, \qquad (A10)$$

$$\boldsymbol{C}_{n_x-1-1/2,j,k}^{-} = \boldsymbol{C}_{n_x-2,j,k} + \frac{\Delta x}{2}\left(\frac{\partial\boldsymbol{C}}{\partial x}\right)_{n_x-2,j,k}, \qquad (A11)$$
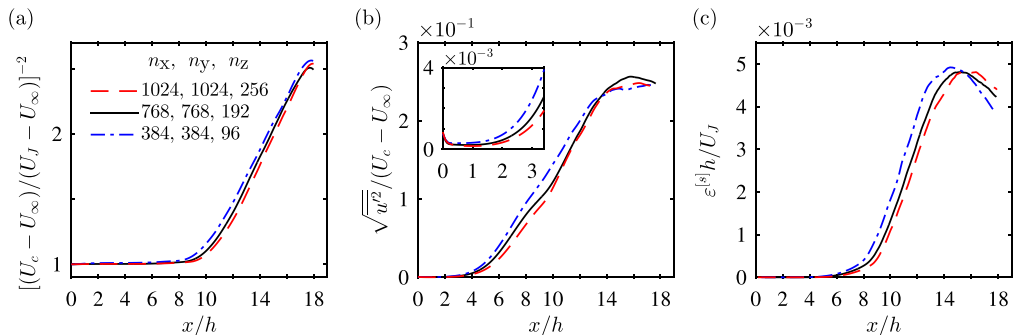
FIG. 21. Streamwise evolution of normalized statistics from three DNS of Newtonian jets with thin shear-layers ($h/\Phi = 40$) that use different number of grid points on each direction, n_x, n_y, and n_z, assessing the influence of mesh resolution on the results: (a) mean velocity, (b) perturbation velocity, and (c) solvent viscous dissipation rate.

for the control volumes centered at $x = L_x - \Delta x$, where the streamwise derivatives are calculated using first-order backward finite differences.

Equations (A5)–(A8) correspond to the Kurganov-Tadmor formulation in a first-order configuration, whereas Eqs. (A9)–(A11) correspond to the Kurganov-Tadmor formulation in a second-order configuration and the condition given by Eq. (A4) has been imposed as boundary condition. This outlet condition allows the exit of the conformation tensor structures without distortion, as can be seen clearly in Fig. 17.

APPENDIX B: MESH RESOLUTION STUDY

The impact of mesh resolution has been assessed by comparing results of the DNS used in the main body of the paper and new simulations that use different values of the grid spacing of the uniform mesh, Δx. This was done by changing the number of grid points on each space direction (n_x, n_y, and n_z), while the remaining parameters were kept unchanged. The results for Newtonian jets are discussed first, in Appendix B 1, while Appendix B 2 deals with the viscoelastic simulations. The results are discussed in physical space, but the same conclusions were obtained in Fourier space.

1. Newtonian jets

For jets with thin shear-layers ($h/\Phi = 40$), three DNS that use $n_x = n_y = 4n_z = 384$, 768, and 1024 were considered, i.e., we compare the reference DNS of the paper with one DNS whose grid spacing is coarser by a factor of two, and a finer mesh DNS where the grid spacing is refined by a factor of $1024/768 \approx 1.33$. For jets with thick shear-layers ($h/\Phi = 5$), we also consider three different cases, with $n_x = n_y = 4n_z = 384$, 768, and 1152, for a fixed domain length of $L_x = L_y = 4L_z = 36h$, i.e., we compare a simulation with the same resolution of the reference DNS analyzed in the main text with two additional DNS that use coarser meshes, with grid spacing larger by factors of $1152/768 = 1.5$ and $1152/384 = 3$.

The results are displayed in Figs. 21 and 22 for thin and thick shear-layers, respectively. The figures show the streamwise evolution of the normalized mean and perturbation velocities, and the mean rate of dissipation of turbulent kinetic energy of the solvent, evaluated at the centerline. For all cases the results are virtually unaffected by the grid spacing. This is true not only for quantities characteristic of the large scale flow structures, such as mean and perturbation velocities, but also for the dissipation $\varepsilon^{[s]}$, whose dynamics are predominant at the smallest scales of the flow and therefore need finer resolution to be captured. Even the simulations with the coarsest mesh exhibit relative differences that are everywhere smaller than 6%, which shows that the Newtonian reference
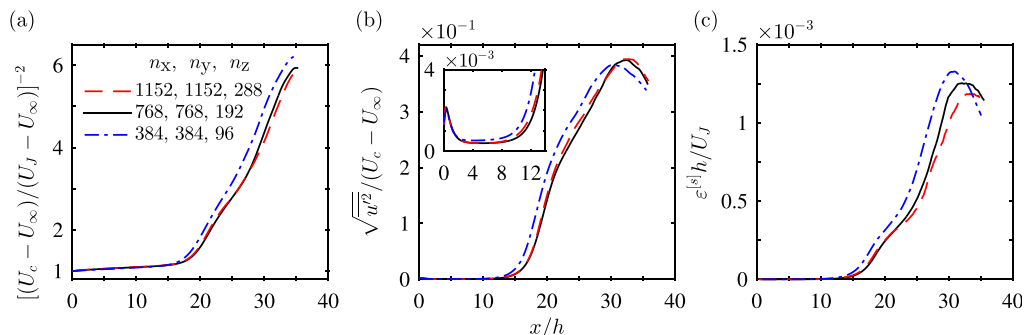
FIG. 22. Streamwise evolution of normalized statistics from three DNS of Newtonian jets with thick shear-layers ($h/\Phi = 5$) that use different number of grid points on each direction, n_x, n_y, and n_z, assessing the influence of mesh resolution on the results: (a) mean velocity, (b) perturbation velocity, and (c) solvent viscous dissipation rate.

DNS discussed in the body of the paper use grid spacings that are much more refined than actually needed, by a factor of at least two, for thin shear-layers, and at least three for thick shear-layers.

2. Viscoelastic jets

For viscoelastic jets we conducted simulations with $n_x = n_y = 4n_z = 512$, 768, and 1024, for Wi $= 2$. At the nonlinear region of transition and at the fully turbulent far-field, i.e., at $x/h \gtrsim 4$ and $x/h \gtrsim 14$, respectively, the mean and perturbation components of velocity obtained from the three DNS are virtually the same [Figs. 23(a) and 23(b)], attesting that the grid spacing is sufficiently small. The same holds true at the linear region of transition, but only for the two DNS with finer resolutions, whereas the coarser DNS at $n_x = n_y = 4n_z = 512$ is poorly resolved at the linear region [inset of Fig. 23(b)]. The dissipation rate obtained from the coarser DNS is slightly underestimated at the turbulent far-field [Fig. 23(c)] but follows the same qualitative behavior of the finer grid simulations. The conclusion is that the viscoelastic DNS analyzed in the body of the paper, with $n_x = n_y = 4n_z = 768$, is well resolved at all regions of the flow.

This conclusion is corroborated by the inspection of the centerline and maximum absolute values of the mean conformation tensor components, shown at Fig. 24. The centerline values
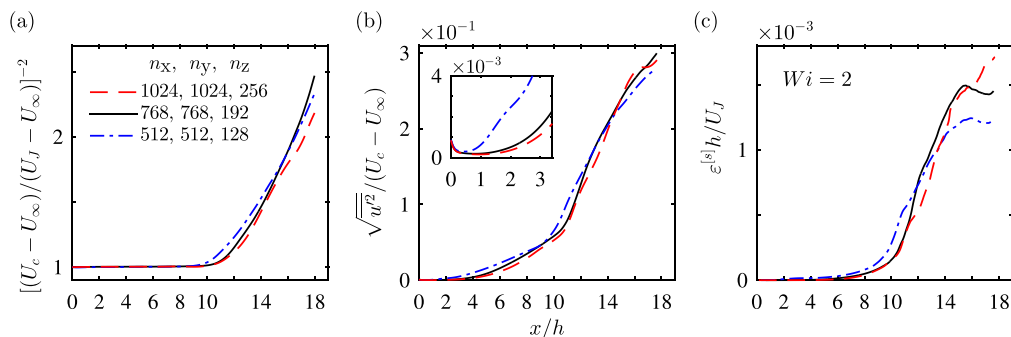

FIG. 23. Streamwise evolution of normalized statistics from three DNS of viscoelastic jets with thin shear-layers ($h/\Phi = 40$) and Wi $= 2$ that use different number of grid points on each direction, n_x, n_y, and n_z, assessing the influence of mesh resolution on the results: (a) mean velocity, (b) perturbation velocity, and (c) solvent viscous dissipation rate.
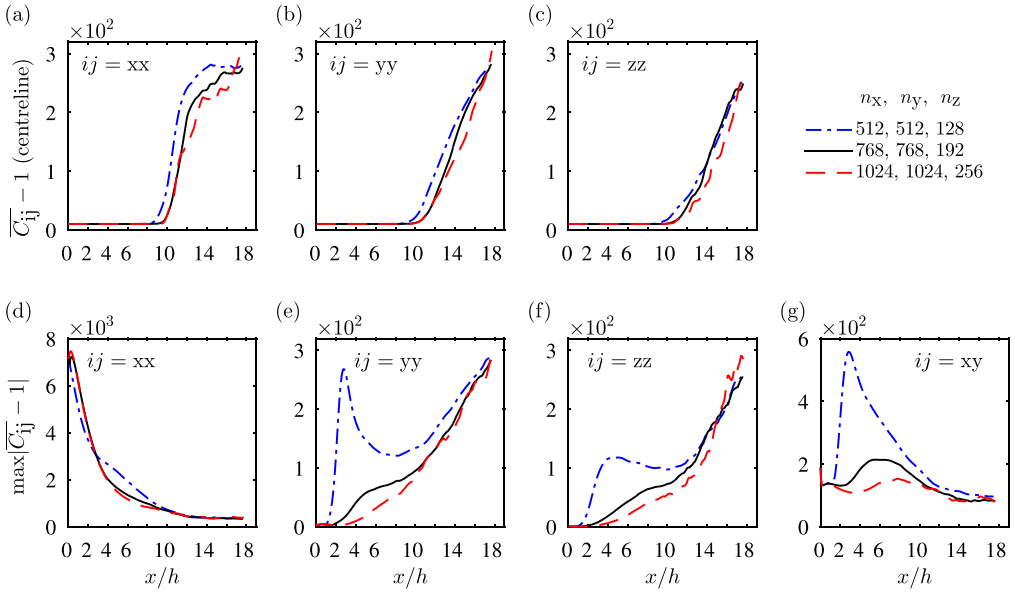
FIG. 24. Streamwise evolution of mean conformation tensor components from three DNS of viscoelastic jets with thin shear-layers ($h/\Phi = 40$) and Wi $= 2$ that use different number of grid points on each direction, n_x, n_y, and n_z: [(a)–(c)] normal components at the centerline, [(d)–(f)] at the position where their values are maximum, and (g) maximum shear component.

start to grow only at the fully turbulent region, and there even the DNS with the coarser mesh ($n_x = n_y = 4n_z = 512$) gives accurate predictions of the conformation tensor [Fig. 24(a)–24(c)]. This is also true for max$|\overline{C_{ij}}|$ [Fig. 24(d)–24(g) at $x/h \gtrsim 12$]. However, at the transition region of the flow the viscoelastic DNS with the coarsest mesh is not able to predict the evolution of max$|\overline{C_{yy}}|$, max$|\overline{C_{zz}}|$, and max$|\overline{C_{xy}}|$, not even qualitatively [Fig. 24(e)–24(g) at $0 \lesssim x/h \lesssim 12$]. Only the largest and therefore the most important max$|\overline{C_{xx}}|$ component is well predicted everywhere by the coarsest DNS with $n_x = n_y = 4n_z = 512$ [Fig. 24(d)]. In contrast, the viscoelastic simulation that uses $n_x = n_y = 4n_z = 768$ is able to predict the evolution of all components of the conformation
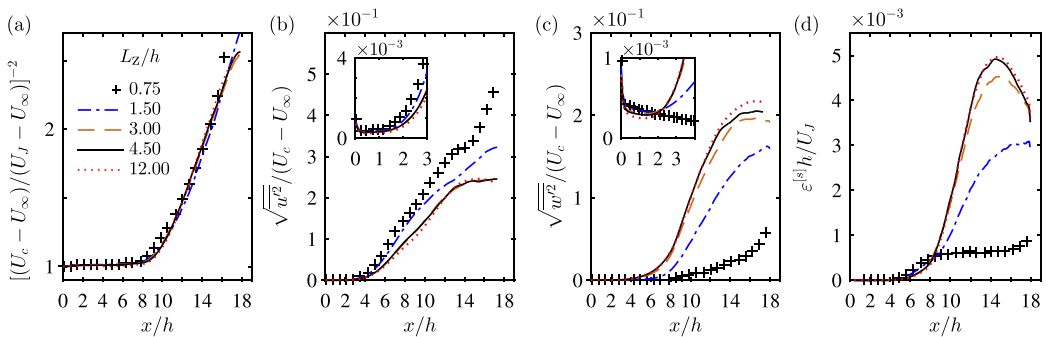

FIG. 25. Streamwise evolution of normalized statistics from five DNS of Newtonian jets with thin shear-layers ($h/\Phi = 40$) that use different domain widths L_z/h and n_z, at the same mesh resolution: (a) mean velocity; [(b) and (c)] perturbation velocities, and (d) solvent viscous dissipation rate.

tensor, at both the transition and fully turbulent regions, attesting once again that this simulation is well resolved.

APPENDIX C: ASSESSMENT OF THE SIZES L_x, L_y, AND L_z USED IN THE SIMULATIONS

We performed numerical tests to validate the domain sizes used in our DNS. This was done by comparing results obtained from simulations that use the same grid resolution (fixed $\Delta x/h$) and different values of L_x/h, L_y/h, and L_z/h, which is achieved by proportionately changing the number of grid points in each direction. The tests were conducted for jets with both thin and thick shear-layers, corresponding to $h/\Phi = 40$ and 5, respectively. Due to computational constraints, the tests were done for Newtonian jets only and use grid spacings that are coarser than those used in the core of this work, since it was shown in Appendix B that those grid resolutions are already sufficiently fine for Newtonian simulations. The results for $h/\Phi = 40$ are discussed first, followed by those obtained from jets with $h/\Phi = 5$.

In order to verify that the domain width L_z/h of the DNS at Re = 1500 and $h/\Phi = 40$ is sufficiently large, we performed five new simulations that use $n_x = n_y = 384$ and $L_x/h = L_y/h = 18$, while the values of the nondimensional domain width are $L_z/h = 0.75$, 1.5, 3, 4.5, and 12, with corresponding n_z given by $n_z = 16$, 32, 64, 96, and 256, respectively. The results are shown in Fig. 25. It is clear that the cases with $L_z/h = 0.75$ and 1.5 are confined on the z direction, since very large changes on some statistics can be observed when we increase L_z/h from 0.75 to 1.5, and from 1.5 to 3. The effect of confinement on the z direction is to increase the values of $\sqrt{\overline{u'^2}}/(U_c - U_\infty)$ and $\sqrt{\overline{v'^2}}/(U_c - U_\infty)$ and to considerably suppress $\sqrt{\overline{w'^2}}/(U_c - U_\infty)$ and ε. For example, at $x/h = 15$ the nondimensional dissipation rate is $\varepsilon h/U_J = 0.64$, 3.03, and 4.48 for the cases with $L_z/h = 0.75$, 1.5, and 3, respectively, and the normalized spanwise rms velocity is $\sqrt{\overline{w'^2}}/(U_c - U_\infty) = 0.28$, 1.4, and 1.95 for the same cases. In contrast, the cases with $L_z/h = 4.5$ and $L_z/h = 12$ show virtually no differences, attesting that the domain width of the DNS analyzed in the body of the paper, $L_z/h = 4.5$, is sufficiently large. In fact, even the case with $L_z/h = 3$ appears to be sufficiently large.

A similar test was carried out to verify that the computational domain length L_x and height L_y are sufficiently large by comparing results from simulations that use $L_x/h = L_y/h = 18$ and 36, with $n_x = n_y = 384$ and 768, respectively. The Reynolds number is Re = 1500 and $h/\Phi = 40$, while $L_z/h = 4.5$ and $n_z = 96$ for both DNS. The results are displayed in Fig. 26 and show that the normalized mean and perturbation velocities and dissipation rate of turbulent kinetic of the
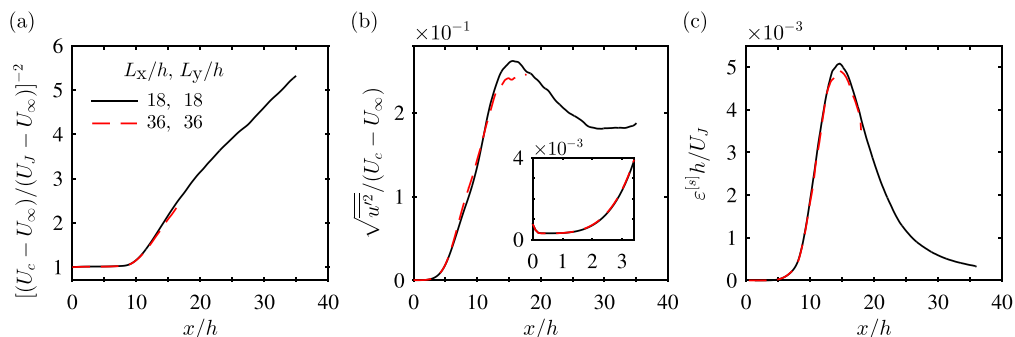

FIG. 26. Streamwise evolution of normalized statistics from two DNS of Newtonian jets with thin shear-layers ($h/\Phi = 40$) that use different domain lengths L_x/h and heights L_y/h, at the same mesh resolution: (a) mean velocity, (b) perturbation velocity, and (c) solvent viscous dissipation rate.
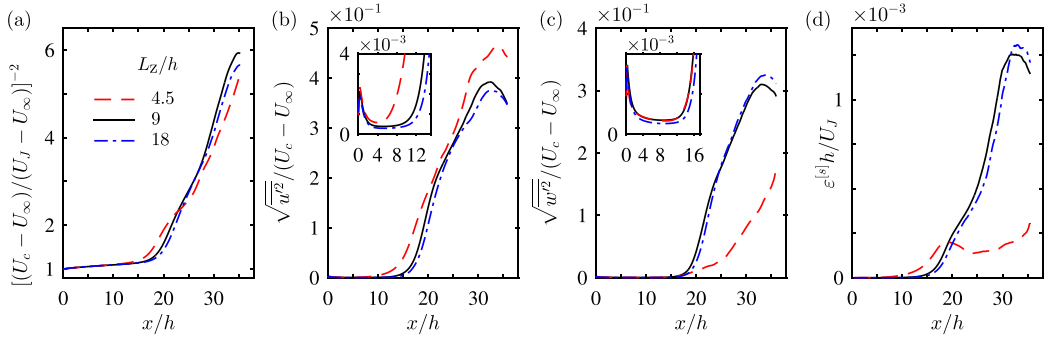
FIG. 27. Streamwise evolution of normalized statistics from three DNS of Newtonian jets with thick shear-layers ($h/\Phi = 5$) that use different domain widths L_z/h and n_z at the same mesh resolution: (a) mean velocity, [(b) and (c)] perturbation velocities, and (d) solvent viscous dissipation rate.

solvent that are obtained from the two simulations are nearly indistinguishable, confirming that $L_x/h = L_y/h = 18$ is sufficiently large.

The validation study of the domain sizes was also performed for jets with thick shear-layers, i.e., jets with $h/\Phi = 5$. To validate the domain width L_z/h, three simulations that use $L_z/h = 4.5$, 9, and 18, with corresponding n_z given by $n_z = 96$, 192, and 384, respectively, and $L_x/h = L_y/h = 36$, $n_x = n_y = 768$, Re = 1500, were considered. The description of the results, shown in Fig. 27, follows similar lines of that for thin shear-layers, but for thick shear-layers a larger domain width $L_z/h = 9$ has to be used to avoid confinement effects. A possible explanation for this is the fact that, for $h/\Phi = 5$, the mean velocity profile at the inlet decays to zero only at $y/h \approx 1$, instead of $y/h \approx 0.5$ (see Fig. 2), suggesting that for this case the length scale that better characterizes the jet slot width is $2h$, instead of h.

To validate the domain length L_x and height L_y used for thick shear-layer jets with $h/\Phi = 5$, we compared the results of two DNS that use $L_x/h = L_y/h = 36$ and 48, with $n_x = n_y = 1152$ and 1536, respectively, while $L_z/h = 9$ and $n_z = 288$ for both simulations. The results, displayed in Fig. 28, demonstrate that $L_x/h = L_y/h = 36$ is sufficiently large.
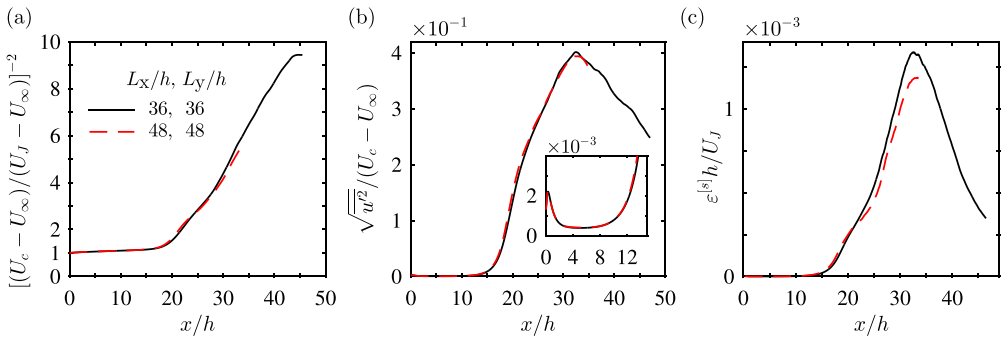

FIG. 28. Streamwise evolution of normalized statistics from two DNS of Newtonian jets with thick shear-layers ($h/\Phi = 5$) that use different domain lengths L_x/h and heights L_y/h at the same mesh resolution: (a) mean velocity, (b) perturbation velocity, and (c) solvent viscous dissipation rate.
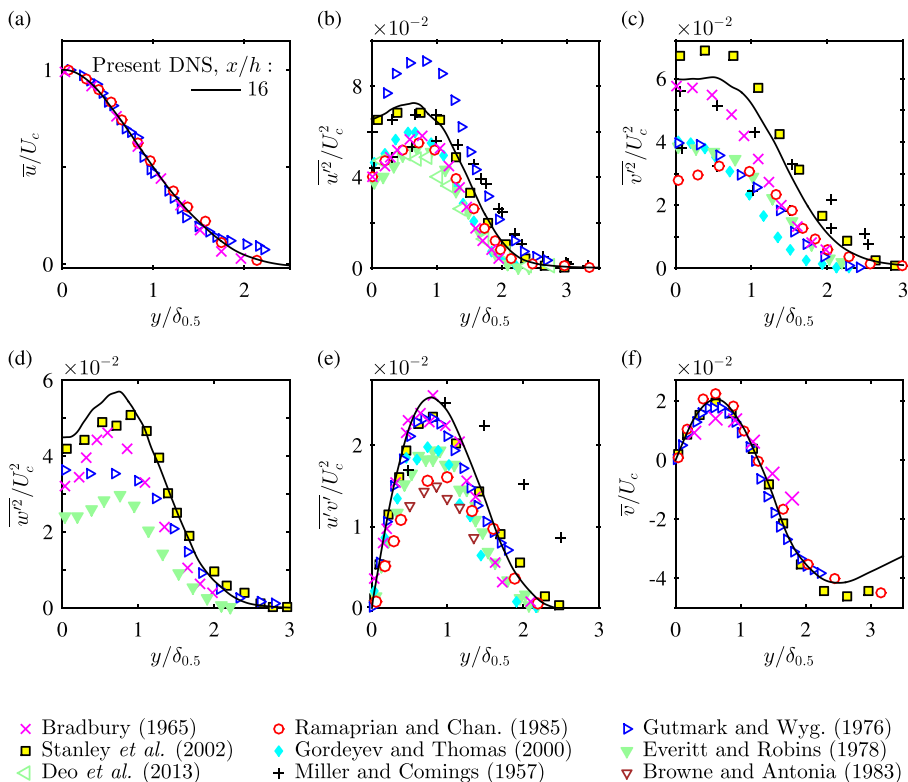
FIG. 29. Transverse profiles of the Reynolds stress and mean velocity components at the fully turbulent far-field region of a Newtonian planar jet normalized as in the classical theory. The results are compared with numerical and experimental data available from the literature.

APPENDIX D: COMPARISONS BETWEEN EXPERIMENTAL AND DNS DATA AT THE FULLY-TURBULENT FAR-FIELD

Several comparisons between our DNS data and experimental results from the literature at the transitioning region of the flow were already presented through the main core of the paper. Figure 29 shows additional comparisons at the fully turbulent far-field region. Transverse profiles of all mean velocity and Reynolds stress components at $x/h = 16$ are compared to the experimental data of Miller and Comings [71], Bradbury [54], Gutmark and Wygnanski [72], Everitt and Robins [55], Browne and Antonia [73], Ramaprian and Chandrasekhara [74], Gordeyev and Thomas [75], Deo *et al.* [76], and to the DNS data of Stanley *et al.* [29]. Good agreement is observed, attesting that our simulations are large enough to attain a fully turbulent condition at the far-field and therefore cover all transition region of the jet.

[1] J. Azaiez and G. M. Homsy, Linear stability of free shear flow of viscoelastic liquids, J. Fluid Mech. **268**, 37 (1994).

[2] J. M. Rallison and E. J. Hinch, Instability of a high-speed submerged elastic jet, J. Fluid Mech. **288**, 311 (1995).

[3] P. K. Ray and T. A. Zaki, Absolute instability in viscoelastic mixing-layers, Phys. Fluids **26**, 014103 (2014).

[4] P. K. Ray and T. A. Zaki, Absolute/convective instability of planar viscoelastic jets, Phys. Fluids **27**, 014110 (2015).

[5] S. Kumar and G. M. Homsy, Direct numerical simulation of hydrodynamic instabilities in two- and three-dimensional viscoelastic free shear-layers, J. Non-Newton Fluid Mech. **83**, 249 (1999).

[6] S. Yamani, B. Keshavarz, Y. Raj, T. A. Zaki, G. H. McKinley, and I. Bischofberger, Spectral universality of elastoinertial turbulence, Phys. Rev. Lett. **127**, 074501 (2021).

[7] S. Yamani, Y. Raj, T. A. Zaki, G. H. McKinley, and I. Bischofberger, Spatiotemporal signatures of elastoinertial turbulence in viscoelastic planar jets, Phys. Rev. Fluids **8**, 064610 (2023).

[8] M. C. Guimarães, N. Pimentel, F. T. Pinho, and C. B. da Silva, Direct numerical simulations of turbulent viscoelastic jets, J. Fluid Mech. **899**, A11 (2020).

[9] M. C. Guimarães, F. T. Pinho, and C. B. da Silva, Turbulent planar wakes of viscoelastic fluids analysed by direct numerical simulations, J. Fluid Mech. **946**, A26 (2022).

[10] G. Howells, Super-Water [R] jetting applications from 1974 to 1999, in *Proceedings of the 10th American Waterjet Conference* (Water Jet Technology Association, St. Louis, USA, 1999), pp. 105–115.

[11] M. Annoni, M. Monno, V. Bertola, and M. Goletti, The role of polymeric additives in water jet cutting, Int J Machin Machinabil Mater **6**, 285 (2009).

[12] D. Hu, C. L. Tang, Y. Kang, and X. Li, An investigation on cutting quality by adding polymer in abrasive water jet, Part. Sci. Technol. **34**, 352 (2016).

[13] Union Carbide Corporation, Anon. Slippery water cuts friction loss. Fire Eng. **122**, 48 (1969); As cited in Sellin *et al.* (1982).

[14] R. H. J. Sellin, J. W. Hoyt, J. Poliert, and O. Scrivener, The effect of drag reducing additives on fluid flows and their industrial applications part 2: Present applications and future proposals, J. Hydraul. Res. **20**, 235 (1982).

[15] H. J. S. Canham, J. P. Catchpole, and R. F. Long, Boundary layer additives to reduce ship resistance, The Naval Architect **2**, 187–213 (1971).

[16] K. Gasljevic and E. F. Matthys, Ship drag reduction by microalgal biopolymers: A feasibility analysis, J. Ship Res. **51**, 326 (2007).

[17] E. D. Burger, W. R. Munk, and H. A. Wahl, Flow increase in the trans Alaska pipeline through use of a polymeric drag-reducing additive, J. Pet. Technol. **34**, 377 (1982).

[18] E. F. Matthys, Heat transfer, drag reduction, and fluid characterization for turbulent flow of polymer solutions: Recent results and research needs, J. Non-Newton. Fluid Mech. **38**, 313 (1991).

[19] R. B. Bird, P. J. Dotson, and N. L. Johnson, Polymer solution rheology based on a finitely extensible bead-spring chain model, J. Non-Newton. Fluid Mech. **7**, 213 (1980).

[20] R. Sureshkumar, A. N. Beris, and R. A. Handler, Direct numerical simulation of the turbulent channel flow of a polymer solution, Phys. Fluids **9**, 743 (1997).

[21] C. Canuto, M. Y. Hussaini, A. Quarteroni, and T. A. Zang, *Spectral Methods in Fluid Dynamics*, 1st ed. (Springer-Verlag, Berlin, 1987).

[22] S. K. Lele, Compact finite difference schemes with spectral-like resolution, J. Comput. Phys. **103**, 16 (1992).

[23] J. H. Williamson, Low-storage Runge-Kutta schemes, J. Comput. Phys. **35**, 48 (1980).

[24] J. Kim and P. Moin, Application of a fractional-step method to incompressible Navier-Stokes equations, J. Comput. Phys. **59**, 308 (1985).

[25] T. Vaithianathan, A. Robert, J. G. Brasseur, and L. R. Collins, An improved algorithm for simulating three-dimensional, viscoelastic turbulence, J. Non-Newton. Fluid Mech. **140**, 3 (2006).

[26] A. Kurganov and E. Tadmor, New high-resolution central schemes for nonlinear conservation laws and convection-diffusion equations, J. Comput. Phys. **160**, 241 (2000).

[27] I. Orlanski, A simple boundary condition for unbounded hyperbolic flows, J. Comput. Phys. **21**, 251 (1976).

[28] P. A. Davidson, *Turbulence, an Introduction for Scientists and Engineers* (Oxford University Press, Oxford, 2004).

[29] S. Stanley, S. Sarkar, and J. P. Mellado, A study of the flow-field evolution and mixing in a planar turbulent jet using direct numerical simulation, J. Fluid Mech. **450**, 377 (2002).

[30] A. Michalke, On spatially growing disturbances in an inviscid shear-layer, J. Fluid Mech. **23**, 521 (1965).

[31] P. Freymuth, On transition in a separated laminar boundary layer, J. Fluid Mech. **25**, 683 (1966).

[32] R. W. Miksad, Experiments on the nonlinear stages of free-shear-layer transition, J. Fluid Mech. **56**, 695 (1972).

[33] P. A. Monkewitz and P. Huerre, Influence of the velocity ratio on the spatial instability of mixing, Phys. Fluids **25**, 1137 (1982).

[34] C. B. da Silva and O. Métais, Vortex control of bifurcating jets: A numerical study, Phys. Fluids **14**, 3798 (2002).

[35] C. B. da Silva and O. Métais, On the influence of coherent structures upon interscale interactions in turbulent plane jets, J. Fluid Mech. **473**, 103 (2002).

[36] C. B. da Silva, D. C. Lopes, and V. Raman, The effect of subgrid-scale models on the entrainment of a passive scalar in a turbulent planar jet, J. Turbul. **16**, 342 (2015).

[37] F. T. Pinho, C. F. Li, B. A. Younis, and R. Sureshkumar, A low Reynolds number turbulence closure for viscoelastic fluids, J. Non-Newton. Fluid Mech. **154**, 89 (2008).

[38] G. K. Batchelor and A. E. Gill, Analysis of the stability of axisymmetric jets, J. Fluid Mech. **14**, 529 (1962).

[39] A. Michalke, Survey on jet instability theory, Prog. Aeronaut. Sci. **21**, 159 (1984).

[40] See Supplemental Material at http://link.aps.org/supplemental/10.1103/PhysRevFluids.8.103301 for the movies showing the two-dimensional contours of the instantaneous vorticity magnitude at the middle plane for a Newtonian and for a viscoelastic jet.

[41] G. E. Mattingly Jr. and W. O. Criminale, Disturbance characteristics in a plane jet, Phys. Fluids **14**, 2258 (1971).

[42] H. Sato, The stability and transition of a two-dimensional jet, J. Fluid Mech. **7**, 53 (1960).

[43] R. A. Antonia, L. W. B. Browne, S. Rajagopalan, and A. J. Chambers, On the organized motion of a turbulent plane jet, J. Fluid Mech. **134**, 49 (1983).

[44] F. O. Thomas and V. W. Goldschmidt, Structural characteristics of a developing turbulent planar jet, J. Fluid Mech. **163**, 227 (1986).

[45] F. O. Thomas and K. M. K. Prakash, An investigation of the natural transition of an untuned planar jet, Phys. Fluids A **3**, 90 (1991).

[46] L. Rayleigh, On the stability, or instability, of certain fluid motions, Proc. Lond. Math. Soc. **s1-11**, 57 (1879).

[47] F. Sausset, O. Cadot, and S. Kumar, Experimental observation of frequency doubling in a viscoelastic mixing-layer, C. R. Mec. **332**, 1001 (2004).

[48] F. O. Thomas and H. C. Chu, An experimental investigation of the transition of the planar jet: Subharmonic suppression and upstream feedback, Phys. Fluids A **1**, 1566 (1989).

[49] K. Oberleithner, L. Rukes, and J. Soria, Mean flow stability analysis of oscillating jet experiments, J. Fluid Mech. **757**, 1 (2014).

[50] C. M. Ho and L. S. Huang, Subharmonics and vortex merging in mixing-layers, J. Fluid Mech. **119**, 443 (1982).

[51] R. W. Miksad, Experiments on free shear layer transition, Ph.D. thesis, Massachusetts Institute of Technology, 1970.

[52] D. Bechert and E. Pfizenmaier, On wavelike perturbations in a free jet travelling faster than the mean flow in the jet, J. Fluid Mech. **72**, 341 (1975).

[53] R. E. Drubka, Instabilities in near field of turbulent jets and their dependence on initial conditions and reynolds number, Ph.D. thesis, Illinois Institute of Technology, 1981.

[54] L. J. S. Bradbury, The structure of a self-preserving turbulent plane jet, J. Fluid Mech. **23**, 31 (1965).

[55] K. W. Everitt and A. G. Robins, The development and structure of turbulent plane jets, J. Fluid Mech. **88**, 563 (1978).

[56] J. W. Oler, Coherent structures in the similarity region of a two-dimensional turbulent jet: A vortex street, Ph.D. thesis, School of Mechanical Engineering, Purdue University, 1980.

[57] J. Cervantes de Gortari and V. W. Goldschmidt, The apparent flapping motion of a turbulent plane jet-Further experimental results, J. Fluids Eng. **103**, 119 (1980).

[58] R. A. Antonia, A. J. Chambers, D. Britz, and L. W. B. Browne, Organized structures in a turbulent plane jet: Topology and contribution to momentum and heat transport, J. Fluid Mech. **172**, 211 (1986).

[59] F. O. Thomas and E. G. Brehob, An investigation of large-scale structure in the similarity region of a two-dimensional turbulent jet, Phys. Fluids **29**, 1788 (1986).

[60] D. G. Crighton and M. Gaster, Stability of slowly diverging jet flow, J. Fluid Mech. **77**, 397 (1976).

[61] K. Gudmundsson and T. Colonius, Instability wave models for the near-field fluctuations of turbulent jets, J. Fluid Mech. **689**, 97 (2011).

[62] S. S. Datta, A. M. Ardekani, P. E. Arratia, A. N. Beris, I. Bischofberger, G. H. McKinley, J. G. Eggers, J. E. López-Aguilar, S. M. Fielding, A. Frishman, M. D. Graham, J. S. Guasto, S. J. Haward, A. Q. Shen, S. Hormozi, A. Morozov, R. J. Poole, V. Shankar, E. S. G. Shaqfeh, H. Stark *et al.*, Perspectives on viscoelastic flow instabilities and elastic turbulence, Phys. Rev. Fluids **7**, 080701 (2022).

[63] J. C. R. Hunt, A. A. Wray, and P. Moin, *Eddies, Stream, and Convergence Zones in Turbulent Flows*, annual research briefs, Proceedings of the Summer Program 1988 (Center for Turbulence Research, Stanford, CA, 1988).

[64] R. B. Bird, R. C. Armstrong, and O. Hassager, *Dynamics of Polymeric Liquids. Volume 1: Fluid Mechanics* (John Wiley & Sons, New York, 1987).

[65] R. G. Larson, E. S. G. Shaqfeh, and S. J. Muller, A purely elastic instability in Taylor-Couette flow, J. Fluid Mech. **218**, 573 (1990).

[66] G. H. McKinley, P. Pakdel, and A. Öztekin, Rheological and geometric scaling of purely elastic flow instabilities, J. Non-Newton. Fluid Mech. **67**, 19 (1996).

[67] J. Page and T. A. Zaki, The dynamics of spanwise vorticity perturbations in homogeneous viscoelastic shear flow, J. Fluid Mech. **777**, 327 (2015).

[68] C. B. da Silva, The role of coherent structures in the control and interscale interactions of round, plane and coaxial jets, Ph.D. thesis, Institut National Polytechnique Grenoble, 2001.

[69] R. J. N. dos Reis, The dynamics of coherent vortices near the turbulent/non-turbulent interface analysed by direct numerical simulations, Ph.D. thesis, Instituto Superior Técnico, 2011.

[70] J. Craske and M. van Reeuwijk, Robust and accurate open boundary conditions for incompressible turbulent jets and plumes, Comput. Fluids **86**, 284 (2013).

[71] D. R. Miller and E. W. Comings, Static pressure distribution in the free turbulent jet, J. Fluid Mech. **3**, 1 (1957).

[72] E. Gutmark and I. Wygnansky, The planar turbulent jet, J. Fluid Mech. **73**, 465 (1976).

[73] L. W. B. Browne and R. A. Antonia, Measurements of turbulent Prandtl number in a plane jet, J. Heat Transf. **105**, 663 (1983).

[74] R. Ramaprian and M. S. Chandrasekhara, LDA measurements in plane turbulent jets, J. Fluids Eng. **107**, 264 (1985).

[75] S. V. Gordeyev and F. O. Tjomas, Coherent structure in the turbulent planar jet. Part 1. Extraction of proper orthogonal decomposition eigenmodes and their self-similarity, J. Fluid Mech. **414**, 145 (2000).

[76] R. C. Deo, J. Mi, and G. J. Nathan, The influence of Reynolds number on a plane jet, Phys. Fluids **20**, 075108 (2008).